# Global Energy Sector Methane Emissions Estimated by using Facility-Level Satellite Observations

**Authors:** Dylan Jervis[1], Marianne Girard[1], Jean-Philippe W MacLean[1], David Marshall[1], Jason McKeever[1], Mathias Strupler[1], Antoine Ramier[1], Ewan Tarrant[1], David Young[1], Joannes D. Maasakkers[2], Ilse Aben[2], and Tia R. Scarpelli[3].

**Affiliations:**

[1]GHGSat Inc, Montreal, QC, Canada

[2]SRON Netherlands Institute for Space Research, Leiden, Netherlands

[3]Carbon Mapper, Pasadena, CA, USA

*Corresponding author. Email: dylan.jervis@ghgsat.com

**Abstract:** Methane emissions from energy sector facilities (oil, gas, and coal) represent a significant contribution to global greenhouse gas emissions with substantial mitigation potential. We estimate global 2023 methane emissions from energy sector point-sources using the high spatial resolution GHGSat satellite constellation. GHGSat detected 8.30$\pm$0.24 Mt yr$^{-1}$ of methane emissions from 3,114 attributed emission sites. Detected O&G and coal emitting sites are found to be emitting 15% and 48% of the time, respectively, without significant continental variation. When comparing to the Global Fuel Exploitation Inventory (GFEIv3), GHGSat's facility-level estimates comprise 12% of GFEIv3's total emissions, or 24% over locations that GHGSat observed at least once, with good spatial correlation at the country scale but only weak spatial correlation at 0.2° x 0.2° grid cell scale.

## Main Text

### Introduction

Methane is the second-most important contributor to global warming behind $CO_2$. The majority of methane emissions originate from anthropogenic sources (*1*) with a significant share of these emissions coming from so-called point-sources – i.e. sources with localized emitting areas commensurate with facility size (order ~100 m). The GHGSat satellite constellation combines high spatial resolution (~25 m), good sensitivity (~100 kg $hr^{-1}$ detection limit), and good coverage (2.4 million square km observed in 2023), allowing for attribution of a substantial fraction of emissions to their point of origin, as well as the revisit frequency to reveal temporal emissions behaviour. Here, we estimate 2023 annual emissions and the average emission persistence of energy sector point-source emission sites across the globe. The 2023 annual emission estimates are made available at 0.2° x 0.2° gridded spatial resolution.

Methane emissions from the energy sector – O&G and coal – have been estimated from both bottom-up inventories and top-down measurements (*2*–*20*). Bottom-up emission estimates typically use ground-based measurements from a small sample of emission sources. Top-down emission estimates, on the other hand, estimate emissions from atmospheric measurements of the methane concentration, typically using aircraft and satellite mounted instruments. Bottom-up estimates are based on knowledge of the underlying activity or process that produces the emission and are therefore indirect estimates of actual methane emissions, and have trouble predicting unexpected emissions and temporal variations. Top-down emission estimates are a more direct estimate of methane emissions, but have typically been limited either in spatio-temporal coverage (e.g. aircraft campaigns conducted over the span of weeks in a certain region (*6*, *7*, *10*, *11*, *21*)) or, if they have more extended spatial coverage and correspondingly coarser spatial resolution (e.g. area flux mappers like TROPOMI), can only coarsely attribute point-source emissions (*22*), or employ inversion techniques that require prior information about emission locations (*2*, *3*). Recently, hybrid top-down bottom-up inventories have been developed for some O&G producing regions (*23*–*25*). A comparison of top-down and bottom-up estimates at different scales can improve our understanding of the process and methods used to produce both estimates.

Emission estimates from satellite point-source and multispectral imagers (e.g. GHGSat, Carbon Mapper, PRISMA, EnMAP, EMIT, Sentinel-2, Landsat) are able to directly attribute emissions on the ~100 m scale (*10*, *13*, *17*, *26*–*30*). They will, however, miss small or diffuse emissions below the instrument's detection limit (GHGSat has a 50% probability of detection of 117 kg/hr at 3 m/s wind speed (*31*, *32*)). Because of the fundamental trade-off between spatial resolution and coverage, a large constellation of point-source imagers is required to approach the spatiotemporal coverage capabilities of a single area flux mapper. A constellation of point-source imagers can achieve near-daily snapshot measurements of a source, building a time series of emissions. As methane sources in the energy sector can be highly variable, estimating the average emission rate from a given location over a period of months or years requires that multiple snapshot satellite measurements taken over extended time periods be aggregated. We construct an emission time series of a site via a spatial aggregation procedure: if an (O&G, coal) plume has an estimated origin location that is within (300 m, 2 km) of another plume detected at a different time, we deem the plumes to be originating from the same location or site. We let the distance criteria be sector-specific to account for the fact that, for example, a coal site may emit from distributed locations within its kilometer-scale site footprint whereas emissions from an O&G site tend to occur from localized infrastructure. The coal mining sector encompasses both localized vent emissions – of which there may be multiple distributed over the surface of the underground mining operations - and more spread-out open pit mine emissions. Figure 1 shows examples of detected plumes from O&G and coal sites. The Materials and Methods section describes that spatial aggregation procedure in more detail. Observations in which no plumes were detected at a site are also included in the emission time series using knowledge of the observation coverage footprint.

Our annualized point-source emission estimate relies on an estimate of the emitting site's emission persistence – the fraction of observations in which a plume is detected at the location. In this way, we present sector and continent resolved site persistence distributions. We compare the GHGSat emission estimates to the most recent global spatially gridded energy sector methane inventory – the recently updated Global Fuel Exploitation Inventory (GFEIv3)(*33*) - at the spatial resolution of GHGSat measurement domains, as well as at the national and global level, providing a unique picture of emissions from the energy sector that is complementary to other top-down and bottom-up estimates. As GFEIv3 country-scale emissions align with the national inventories reported to the UNFCCC, our comparison at the country-scale has implications for these policy-relevant inventories.

## Temporal Emissions Behaviour

The results presented in this paper are derived from 32,928 clear-sky observations, 14,137 of which were taken over O&G or coal sites that were observed to be emitting by GHGSat in 2023. A total of 11,419 detected plumes have been attributed to 3,114 distinct O&G or coal sites alongside "null" observations of these sites in which the site was observed in clear-sky conditions, but no plumes were detected. On average, GHGSat made (26,17) observations – median of (19, 12) observations - of each emitting (O&G, coal) site during 2023. The average clear-sky revisit time was (10, 16) days – median (5,8) days - for each emitting (O&G, coal) site. A calculation of the temporal autocorrelation of our 2023 site observations (see supplementary materials) shows a slowly decreasing probability of having observed a site as a function of the time between observations, without noticeable periodicity or other temporally correlated features. In many cases, multiple sites were observed within the same observation footprint. See the supplementary materials for a summary of GHGSat measurement details.

The persistence quantifies the fraction of site observations in which a plume is detected at a given location. We use an estimated persistence measure (see Materials and Methods) to account for the sampling bias that occurs when only a few observations of an emitting site have been taken. An emitting site is a site in which at least one emission was detected in $N$ observations. The observed persistence for an emitting site where emissions have been detected in $M$ observations is $M/N$, which is an unreliable estimate when either $M$or $N$ is small, especially for the case of intermittent emitters ($M \ll N$). We therefore use an estimated persistence measure $\langle\hat{p}\rangle = \langle p_o(x)p_p(x)\rangle$ which is defined as the mean of the joint probability distribution between the observed $p_o(x)$ and prior $p_p(x)$ persistence probability distributions. The prior persistence distributions are constructed on a per-sector and per-continent basis from sites that have been observed at least 10 times. Not only does the estimated persistence provide temporal information about sector emissions it is also used to estimate the time-averaged emission rate of a site $\hat{Q} = \langle\hat{p}\rangle\langle Q_{q\neq 0}\rangle$, with $\langle Q_{q\neq 0}\rangle$ being the average emission rate of the detected plumes.

The estimated persistence distributions of sites where GHGSat has detected at least one emission are shown in Figure 2. Figure 2a and 2b show the O&G and coal persistence distribution for each continent, respectively, and Figure 2c shows the average persistence distribution for each sector globally. Figures 2a and 2b suggest that a site's sector is more indicative of its persistence than the continent it is located in: for both O&G and coal, the persistence distributions are largely similar across continents where at least $n$=5 or more sites have been included in the average. Figure 2c shows that O&G sites are much more intermittent (i.e. less persistent) than coal sites: the average estimated persistence is 0.15 for O&G compared to 0.48 for coal. This means that plumes above GHGSat's ~100 kg $hr^{-1}$ detection limit are detected from emitting O&G sites in just 15% of observations, compared to 48% of emitting coal sites. We also note the flat persistence distribution of coal sites: GHGSat satellites are (approximately) equally as likely to observe a very persistent source as they are to observe a very intermittent or semi-persistent source. Our coal persistence estimates are consistent with in situ studies of individual coal ventilation shafts where emission rates were found to vary significantly, including down to negligibly small magnitudes (*34*, *35*)

The measured intermittency of the O&G sector is consistent with the periodic maintenance, leak and repair events that are specific to the sector (*36*, *37*). A remote sensing measurement campaign conducted over the course of 3 months with the AVIRIS-NG aircraft instrument in the Permian basin found O&G sources to be intermittent (*6*) (66% of detected sources had a persistence of 0.25 or less). This is consistent with our results (approximately 80% of emitting O&G sites with persistence <20%), accounting for the fact that the persistence distribution estimated from an instrument with higher detection limit will in general be lower (*38*). The estimated persistence distribution can also depend on the timescale over which observations are aggregated: an AVIRIS-NG study that aggregated results from a series of campaigns found that the site persistence distributions evolved from approximately flat to bi-modal when lengthening the aggregation time period from weeks to a year (*7*).

The fact that O&G site emissions tend to be more intermittent than coal site emissions has implications for the temporal coverage required of each sector to detect emissions. Given that the probability of detecting an emission from a source with persistence $p$ in $N$ observations is $1-(1-p)^N$, assuming binomial emissions behaviour (*39*), it would take ~14 observations to have a 90% chance of detecting an emission from these O&G sites above GHGSat's detection limit compared to only ~4 observations for a coal emission. Similarly for the quantification uncertainty of the time-averaged site emission rate estimate: it requires many more observations of an intermittent emitter to estimate the site emission rate to the same level of statistical precision as a more persistent site.

We further investigate the temporal behaviour of O&G and coal emissions by calculating the temporal autocorrelation function of detected emissions. We find (see supplementary materials) that the probability of detecting an emission at time $\tau$ after having previously detected an emission is approximately constant, and similar to the average persistence value for each sector, for all $\tau$, with the potential exception of O&G sites which seem to have an elevated detection probability at small $\tau$. That is, detected emissions largely appear randomly distributed in time within statistical fluctuations, with the possible exception O&G sites which may exhibit temporally correlated emission behaviour over the timescale of days-to-weeks.

**Comparing GHGSat estimated emissions with GFEI**

We present the spatial distribution of GHGSat observations and estimated emissions at $0.2°$ x $0.2°$ resolution. This spatial gridding approach is chosen because the $0.2°$ x $0.2°$ resolution is approximately equal to the area of a GHGSat retrieval domain, and it allows for a comparison to the spatially gridded GFEIv3 inventory. The GHGSat estimated flux in a grid cell with center lat/lon coordinates $(\lambda, \phi)$ is calculated by summing all estimated site emissions $\hat{Q}$ that are located within $(\lambda \pm 0.1°\ , \phi \pm 0.1°)$, and then dividing by the area that a particular grid cell encompasses. A map of gridded GHGSat emission estimates is shown in Figure 3 for selected regions.

GHGSat estimated emission fluxes are compared with the GFEI inventory over three different spatial scales: globally, country level, and grid-cell level. A map of the difference between GHGSat and GFEIv3 estimated emissions is shown in the supplementary materials. The total GHGSat emissions estimate is $\hat{Q}_{tot}$= 8.30$\pm$0.24 Mt yr$^{-1}$, with 5.80$\pm$0.23 Mt yr$^{-1}$ attributed to O&G sites and 2.50$\pm$0.06 Mt yr$^{-1}$ attributed to coal sites. The GHGSat estimated total represents 11.7% of the total GFEIv3 estimated emissions (74.3 Mt yr$^{-1}$ = 43.7 Mt yr$^{-1}$ O&G + 30.7 Mt yr$^{-1}$ coal). However, given that the GHGSat constellation only has partial coverage of locations where GFEIv3 predicts emissions to be originating from, we also compare GHGSat measured emissions to GFEIv3 only at locations where GHGSat had made at least one successful observation (without necessarily detecting an emission). At these GHGSat observed locations, the GHGSat estimated total represents a larger fraction of the GFEIv3 predicted emissions: 35% of the GFEIv3-predicted 16.4 Mt yr$^{-1}$ for O&G and 14% of the GFEIv3-predicted 17.8 Mt yr$^{-1}$ for coal, and 24% of 34.1 Mt yr$^{-1}$ for both combined. If we assume that the cumulative GFEI emissions predicted at the GHGSat observed locations were accurate, then the GHGSat measured emission fractions could be interpreted as the fraction of emissions observable above GHGSat's ~100 kg $hr^{-1}$ detection limit. This would be roughly consistent with a Permian basin measurement study conducted using an instrument with a 90% probability of detection of 2 kg $hr^{-1}$ (*38*) that estimated that fewer than 35% of total emissions originate from sources above 100 kg $hr^{-1}$. However, it should be noted that national top-down emission estimates using TROPOMI measurements were consistently larger than the 2019 GFEIv2 estimates (*2*).

In comparing GHGSat estimated emission totals to GFEIv3 at GHGSat observed locations, there is the tacit assumption GFEI is accurate in aggregate. To examine this further, we compare GFEI emission estimates to those from GHGSat at GHGSat-observed locations at both individual grid cell resolution, as well as for multiple grid cells aggregated within a country. Figures 4a and 4b show a comparison of GHGSat national emission estimates with those from GFEI, either for the country total (solid points) or only at GHGSat-observed aggregated locations in-country (open points). Qualitatively, we observe a correlation between emission rates predicted by GFEI and those estimated by GHGSat, though the correlation is stronger for the coal sector than for O&G. The correlation can be quantified with both a standard, and emission error-weighted, Pearson correlation coefficient. When calculating the error-weighted correlation coefficient (see Materials and Methods), we use the GHGSat estimated error to weight GHGSat emission estimates and assume zero error for GFEIv3 estimates (as none are provided). Furthermore, because the GHGSat emission error estimate is only defined for locations with non-zero emissions, we only calculate error-weighted correlations over locations with non-zero emissions. The standard correlation coefficients are (0.504, 0.967) for the (O&G, coal) sectors, whereas the error-weighted correlation coefficients are (0.294, 0.714) for the (O&G, coal) sectors. For context, a correlation coefficient of (-1,0,1) would indicate (perfect anti-correlation, zero correlation, perfect correlation) between variables. Therefore, we observe strong correlation for the coal sector between GHGSat emission estimates and GFEIv3 at the country-aggregated scale, and moderate correlation for the O&G sector. The correlations are slightly reduced when using an error-weighted correlation metric, suggesting that the more reliable a GHGSat emission estimate is, the less correlated it is with a GFEIv3 estimate, possibly due to the repeated targeting of outlier locations where large emissions were detected.

We also investigate the correlation between GHGSat and GFEIv3 at the resolution of individual 0.2° x 0.2° grid cells (see Figure 5). The correlation is much weaker compared to the country-aggregated total, with the standard and error-weighted Pearson correlation coefficients equal to (0.224, 0.243) and (0.183, 0.233), respectively, for the (O&G, coal) sectors. That is, the correlation between GHGSat and GFEIv3 estimated emissions is weak-to-negligible at the level of individual grid cells, and with similar values between the O&G and coal sectors. Maps comparing GHGSat and GFEIv3 gridded emission predictions are shown for selected countries in the supplementary materials.

## Discussion

We have produced the first global gridded estimate of annual emissions from measured O&G and coal point sources, enabled by the GHGSat constellation. This annual gridded estimate can help provide a basis for emissions reporting. The GHGSat gridded emission estimates rely on both detected emissions as well as clear-sky non-detections at emission sites via an estimated emissions persistence measure that is informative in its own right: the estimated persistence can inform how frequently a site should be monitored to more accurately detect and quantify its emissions (higher frequency temporal coverage is required for more intermittent emitters); it can be used to constrain an estimate of the average duration of emission events; it can reveal information about operational procedures that may affect emissions, and how they may vary between sectors, regions, season, or even time-of-day; and it can provide bottom-up inventory estimates with novel temporal information with which to better account for emissions. We have shown good agreement between the GHGSat and GFEIv3 coal emission estimates for at the national level, and moderate-to-weak agreement for national O&G emissions, but weak-to-poor agreement at the spatial resolution of individual 0.2° x 0.2° grid cells for both O&G and coal sectors. This suggests that inventory estimates may have trouble accurately estimating emissions at the facility scale.

In presenting our results, it is important to qualify that the site persistence and emission rate estimated by an observing system will depend on the emission rate detection sensitivity of the system. For instance, an instrument with a better emission rate detection sensitivity will generally estimate a larger persistence (*5, 13*). The persistence and emission estimates of a site measured with instruments with different sensitivities can be reconciled using knowledge of the site's emission rate distribution measured using the most sensitive instrument to take advantage of the enhanced coverage from a combined instrument system (*40*).

The number of satellite methane point-source imagers in orbit is expected to grow in the coming years, providing increased spatiotemporal coverage of facility level emissions. Increased spatiotemporal coverage will enable more, and more accurate, site emission and persistence estimates, as well as the improved ability to constrain the duration of individual emission events. However, even a very large constellation of point-source imagers may miss a substantial fraction of emissions (*39*). Therefore, there is promise in integrating point-source measurements more fully into the larger methane remote sensing ecosystem. For example, point-source measurements could help inform emission inversion estimates from coarser spatial resolution systems by providing more accurate prior mean and prior covariance estimates (*41*). Conversely, they can provide valuable tip-and-cue information for more sensitive, higher spatial systems (e.g. airborne and ground-based instruments) for follow-up investigation. The lack of strong per-grid cell agreement between GHGSat estimated emissions and the bottom-up GFEIv3 prediction suggests that a measurement-informed inventory approach could be beneficial.

## References


1. M. Saunois, A. R. Stavert, B. Poulter, P. Bousquet, J. G. Canadell, R. B. Jackson, P. A. Raymond, E. J. Dlugokencky, S. Houweling, P. K. Patra, P. Ciais, V. K. Arora, D. Bastviken, P. Bergamaschi, D. R. Blake, G. Brailsford, L. Bruhwiler, K. M. Carlson, M. Carrol, S. Castaldi, N. Chandra, C. Crevoisier, P. M. Crill, K. Covey, C. L. Curry, G. Etiope, C. Frankenberg, N. Gedney, M. I. Hegglin, L. Höglund-Isaksson, G. Hugelius, M. Ishizawa, A. Ito, G. Janssens-Maenhout, K. M. Jensen, F. Joos, T. Kleinen, P. B. Krummel, R. L. Langenfelds, G. G. Laruelle, L. Liu, T. MacHida, S. Maksyutov, K. C. McDonald, J. McNorton, P. A. Miller, J. R. Melton, I. Morino, J. Müller, F. Murguia-Flores, V. Naik, Y. Niwa, S. Noce, S. O'Doherty, R. J. Parker, C. Peng, S. Peng, G. P. Peters, C. Prigent, R. Prinn, M. Ramonet, P. Regnier, W. J. Riley, J. A. Rosentreter, A. Segers, I. J. Simpson, H. Shi, S. J. Smith, L. Paul Steele, B. F. Thornton, H. Tian, Y. Tohjima, F. N. Tubiello, A. Tsuruta, N. Viovy, A. Voulgarakis, T. S. Weber, M. Van Weele, G. R. Van Der Werf, R. F. Weiss, D. Worthy, D. Wunch, Y. Yin, Y. Yoshida, W. Zhang, Z. Zhang, Y. Zhao, B. Zheng, Q. Zhu, Q. Zhu, Q. Zhuang, The global methane budget 2000-2017. *Earth Syst Sci Data* **12**, 1561–1623 (2020).
2. L. Shen, D. J. Jacob, R. Gautam, M. Omara, T. R. Scarpelli, A. Lorente, D. Zavala-Araiza, X. Lu, Z. Chen, J. Lin, National quantifications of methane emissions from fuel exploitation using high resolution inversions of satellite observations. *Nat Commun* **14**, 4948 (2023).
3. Y. Zhang, R. Gautam, S. Pandey, M. Omara, J. D. Maasakkers, P. Sadavarte, D. Lyon, H. Nesser, M. P. Sulprizio, D. J. Varon, others, Quantifying methane emissions from the largest oil-producing basin in the United States from space. *Sci Adv* **6**, eaaz5120 (2020).
4. T. Lauvaux, C. Giron, M. Mazzolini, A. d'Aspremont, R. Duren, D. Cusworth, D. Shindell, P. Ciais, Global Assessment of Oil and Gas Methane Ultra-Emitters. *arXiv preprint arXiv:2105.06387* (2021).
5. T. Ehret, A. De Truchis, M. Mazzolini, J.-M. Morel, T. Lauvaux, R. Duren, D. Cusworth, G. Facciolo, Global Tracking and Quantification of Oil and Gas Methane Emissions from Recurrent Sentinel-2 Imagery. (2021).
6. D. H. Cusworth, R. M. Duren, A. K. Thorpe, W. Olson-Duvall, J. Heckler, J. W. Chapman, M. L. Eastwood, M. C. Helmlinger, R. O. Green, G. P. Asner, P. E. Dennison, C. E. Miller, Intermittency of Large Methane Emitters in the Permian Basin. *Environ Sci Technol Lett* **8**, 567–573 (2021).
7. D. H. Cusworth, A. K. Thorpe, A. K. Ayasse, D. Stepp, J. Heckler, G. P. Asner, C. E. Miller, V. Yadav, J. W. Chapman, M. L. Eastwood, R. O. Green, B. Hmiel, D. R. Lyon, R. M. Duren, Strong methane point sources contribute a disproportionate fraction of total emissions across multiple basins in the United States. doi: 10.1073/pnas (2022).
9. T. R. Scarpelli, D. J. Jacob, S. Grossman, X. Lu, Z. Qu, M. P. Sulprizio, Y. Zhang, F. Reuland, D. Gordon, J. R. Worden, Updated Global Fuel Exploitation Inventory (GFEI) for methane emissions from the oil, gas, and coal sectors: Evaluation with inversions of atmospheric methane observations. *Atmos Chem Phys* **22**, 3235–3249 (2022).
10. D. J. Varon, J. McKeever, D. Jervis, J. D. Maasakkers, S. Pandey, S. Houweling, I. Aben, T. Scarpelli, D. J. Jacob, Satellite discovery of anomalously large methane point sources from oil/gas production. *Geophys Res Lett* (2019).
11. D. H. Cusworth, R. M. Duren, A. K. Thorpe, S. Pandey, J. D. Maasakkers, I. Aben, D. Jervis, D. J. Varon, D. J. Jacob, C. A. Randles, others, Multisatellite Imaging of a Gas Well Blowout Enables Quantification of Total Methane Emissions. *Geophys Res Lett* **48**, e2020GL090864 (2021).
12. B. J. Schuit, J. D. Maasakkers, P. Bijl, G. Mahapatra, A. W. Van Den Berg, S. Pandey, A. Lorente, T. Borsdorff, S. Houweling, D. J. Varon, J. McKeever, D. Jervis, M. Girard, I. Irakulis-Loitxate, J. Gorroño, L. Guanter, D. H. Cusworth, I. Aben, Automated detection and monitoring of methane super-emitters using satellite data. *Atmos Chem Phys* **23**, 9071–9098 (2023).
13. A. K. Thorpe, R. O. Green, D. R. Thompson, P. G. Brodrick, J. W. Chapman, C. D. Elder, I. Irakulis-Loitxate, D. H. Cusworth, A. K. Ayasse, R. M. Duren, C. Frankenberg, L. Guanter, J. R. Worden, P. E. Dennison, D. A. Roberts, K. D. Chadwick, M. L. Eastwood, J. E. Fahlen, C. E. Miller, "Attribution of individual methane and carbon dioxide emission sources using EMIT observations from space" (2023); https://www.science.org.
14. M. R. Johnson, B. M. Conrad, D. R. Tyner, Creating measurement-based oil and gas sector methane inventories using source-resolved aerial surveys. *Commun Earth Environ* **4** (2023).

15. D. Zavala-Araiza, S. C. Herndon, J. R. Roscioli, T. I. Yacovitch, M. R. Johnson, D. R. Tyner, M. Omara, B. Knighton, D. Helmig, S. Schwietzke, Methane emissions from oil and gas production sites in Alberta, Canada. *Elementa: Science of the Anthropocene* **6** (2018).
16. M. V. Dangeti, M. Pathakoti, K. L. Asuri, S. Peethani, I. Shaik, R. Krishnan Sundara, V. K. Sagar, R. Pushpanathan, Y. K. Tiwari, P. Chauhan, Emissions of methane from coal fields, thermal power plants, and wetlands and their implications for atmospheric methane across the south Asian region. *Atmos Chem Phys* **24**, 12843–12859 (2024).
17. T.-L. He, R. J. Boyd, D. J. Varon ID, A. J. Turner, Increased methane emissions from oil and gas following the Soviet Union's collapse. doi: 10.1073/pnas (2024).
18. J. D. Maasakkers, E. E. McDuffie, M. P. Sulprizio, C. Chen, M. Schultz, L. Brunelle, R. Thrush, J. Steller, C. Sherry, D. J. Jacob, S. Jeong, B. Irving, M. Weitz, A Gridded Inventory of Annual 2012-2018 U.S. Anthropogenic Methane Emissions. *Environ Sci Technol* **57**, 16276–16288 (2023).
19. M. Crippa, D. Guizzardi, F. Pagani, M. Schiavina, M. Melchiorri, E. Pisoni, F. Graziosi, M. Muntean, J. Maes, L. Dijkstra, M. Van Damme, L. Clarisse, P. Coheur, Insights into the spatial distribution of global, national, and subnational greenhouse gas emissions in the Emissions Database for Global Atmospheric Research (EDGAR v8.0). *Earth Syst Sci Data* **16**, 2811–2830 (2024).
20. D. J. Varon, D. J. Jacob, B. Hmiel, R. Gautam, D. R. Lyon, M. Omara, M. Sulprizio, L. Shen, D. Pendergrass, H. Nesser, Z. Qu, Z. R. Barkley, N. L. Miles, S. J. Richardson, K. J. Davis, S. Pandey, X. Lu, A. Lorente, T. Borsdorff, J. D. Maasakkers, I. Aben, Continuous weekly monitoring of methane emissions from the Permian Basin by inversion of TROPOMI satellite observations. *Atmos Chem Phys* **23**, 7503–7520 (2023).
21. S. Pandey, J. Worden, D. H. Cusworth, D. Varon, M. D. Thill, D. J. Jacob, K. W. Bowman, "Relating Multi-Scale Plume Detection and Area Estimates of Methane Emissions: A Theoretical and Empirical Analysis" (2024).
22. T. Lauvaux, C. Giron, M. Mazzolini, A. D'aspremont, R. Duren, D. Cusworth, "Global assessment of oil and gas methane ultra-emitters."
23. M. R. Johnson, B. M. Conrad, D. R. Tyner, Creating measurement-based oil and gas sector methane inventories using source-resolved aerial surveys. *Commun Earth Environ* **4** (2023).
24. B. M. Conrad, D. R. Tyner, H. Z. Li, D. Xie, M. R. Johnson, A measurement-based upstream oil and gas methane inventory for Alberta, Canada reveals higher emissions and different sources than official estimates. *Commun Earth Environ* **4** (2023).
25. E. Chan, F. Vogel, S. Smyth, O. Barrigar, M. Ishizawa, J. Kim, M. Neish, D. Chan, D. E. J. Worthy, Hybrid bottom-up and top-down framework resolves discrepancies in Canada's oil and gas methane inventories. *Commun Earth Environ* **5** (2024).
26. R. Loizzo, R. Guarini, F. Longo, T. Scopa, R. Formaro, C. Facchinetti, G. Varacalli, "PRISMA: The Italian hyperspectral mission" in *IGARSS 2018-2018 IEEE International Geoscience and Remote Sensing Symposium* (2018), pp. 175–178.
27. D. J. Varon, D. Jervis, J. McKeever, I. Spence, D. Gains, D. J. Jacob, High-frequency monitoring of anomalous methane point sources with multispectral Sentinel-2 satellite observations. *Atmos Meas Tech* **14**, 2771–2785 (2021).
28. J. Roger, I. Irakulis-Loitxate, A. Valverde, J. Gorroño, S. Chabrillat, M. Brell, L. Guanter, High-Resolution Methane Mapping with the EnMAP Satellite Imaging Spectroscopy Mission. *IEEE Transactions on Geoscience and Remote Sensing* **62**, 1–12 (2024).
29. D. Jervis, J. McKeever, B. O. A. Durak, J. J. Sloan, D. Gains, D. J. Varon, A. Ramier, M. Strupler, E. Tarrant, The GHGSat-D imaging spectrometer. *Atmos Meas Tech* **14**, 2127–2140 (2021).
30. J. D. Maasakkers, D. J. Varon, A. Elfarsdóttir, J. McKeever, D. Jervis, G. Mahapatra, S. Pandey, A. Lorente, T. Borsdorff, L. R. Foorthuis, B. J. Schuit, P. Tol, T. A. van Kempen, R. van Hees, I. Aben, "Using satellites to uncover large methane emissions from landfills" (2022); https://www.science.org.
31. J. Mckeever, D. Jervis, "Validation and Metrics for Emissions Detection by Satellite" (2022); https://www.ghgsat.com/en/case-studies/validation-and-metrics-for-emissions-detection-by-satellite/.
32. A. Ramier, M. Girard, D. Jervis, J.-P. Maclean, D. Marshall, J. Mckeever, M. Strupler, E. Tarrant, D. Young, "High-Resolution Methane Detection with the GHGSat Constellation" (2023).
33. T. R. Scarpelli, E. Roy, D. J. Jacob, M. P. Sulprizio, R. D. Tate, D. H. Cusworth, Using new geospatial data and 2020 fossil fuel methane emissions for the Global Fuel Exploitation Inventory (GFEI) v3. doi: 10.7910/DVN/HH4EUM.

34. J. Swolkień, A. Fix, M. Gałkowski, Factors influencing the temporal variability of atmospheric methane emissions from Upper Silesia coal mines: a case study from the CoMet mission. *Atmos Chem Phys* **22**, 16031–16052 (2022).
35. T. Andersen, K. Vinkovic, M. de Vries, B. Kers, J. Necki, J. Swolkien, A. Roiger, W. Peters, H. Chen, Quantifying methane emissions from coal mining ventilation shafts using an unmanned aerial vehicle (UAV)-based active AirCore system. *Atmos Environ X* **12** (2021).
36. H. L. Brantley, E. D. Thoma, W. C. Squier, B. B. Guven, D. Lyon, Assessment of methane emissions from oil and gas production pads using mobile measurements. *Environ Sci Technol* **48**, 14508–14515 (2014).
37. A. V. Strizhenok, D. S. Korelskiy, Estimation and reduction of methane emissions at the scheduled and repair outages of gas-compressor units. *Journal of Ecological Engineering* **20**, 46–51 (2019).
38. W. M. Kunkel, A. E. Carre-Burritt, G. S. Aivazian, N. C. Snow, J. T. Harris, T. S. Mueller, P. A. Roos, M. J. Thorpe, Extension of Methane Emission Rate Distribution for Permian Basin Oil and Gas Production Infrastructure by Aerial LiDAR. *Environ Sci Technol* **57**, 12234–12241 (2023).
39. D. J. Jacob, D. J. Varon, D. H. Cusworth, P. E. Dennison, C. Frankenberg, R. Gautam, L. Guanter, J. Kelley, J. McKeever, L. E. Ott, B. Poulter, Z. Qu, A. K. Thorpe, J. R. Worden, R. M. Duren, Quantifying methane emissions from the global scale down to point sources using satellite observations of atmospheric methane. Copernicus GmbH [Preprint] (2022). https://doi.org/10.5194/acp-22-9617-2022.
40. A. K. Ayasse, D. H. Cusworth, K. Howell, K. O'Neill, B. M. Conrad, M. R. Johnson, J. Heckler, G. P. Asner, R. Duren, Probability of Detection and Multi-Sensor Persistence of Methane Emissions from Coincident Airborne and Satellite Observations. *Environ Sci Technol*, doi: 10.1021/acs.est.4c06702 (2024).
41. S. Naus, J. D. Maasakkers, R. Gautam, M. Omara, R. Stikker, A. K. Veenstra, B. Nathan, I. Irakulis-Loitxate, L. Guanter, S. Pandey, M. Girard, A. Lorente, T. Borsdorff, I. Aben, Assessing the Relative Importance of Satellite-Detected Methane Superemitters in Quantifying Total Emissions for Oil and Gas Production Areas in Algeria. *Environ Sci Technol* **57**, 19545–19556 (2023).

**Acknowledgments:** We would like to thank Daniel Jacob and James East for helpful comments during the writing of this manuscript.

**Author contributions:**

Conceptualization: DJ

Methodology: DJ

Investigation: DJ, JDM, JM, MG, IA

Formal analysis: DJ, AR

Data curation: DJ, MG, DY, DM, JPM, DM, JM, MS, AR,

Visualization: DJ

Validation: DJ, JM, MG, BM

Software: DJ, ET, DY, AR

Resources: TS

Writing – original draft: DJ

Writing – review & editing: All authors

**Competing interests:** The authors declare no competing interests.

**Data and materials availability:** Gridded emission estimates and anonymized site emissions data will be made publicly available upon publication of this manuscript.

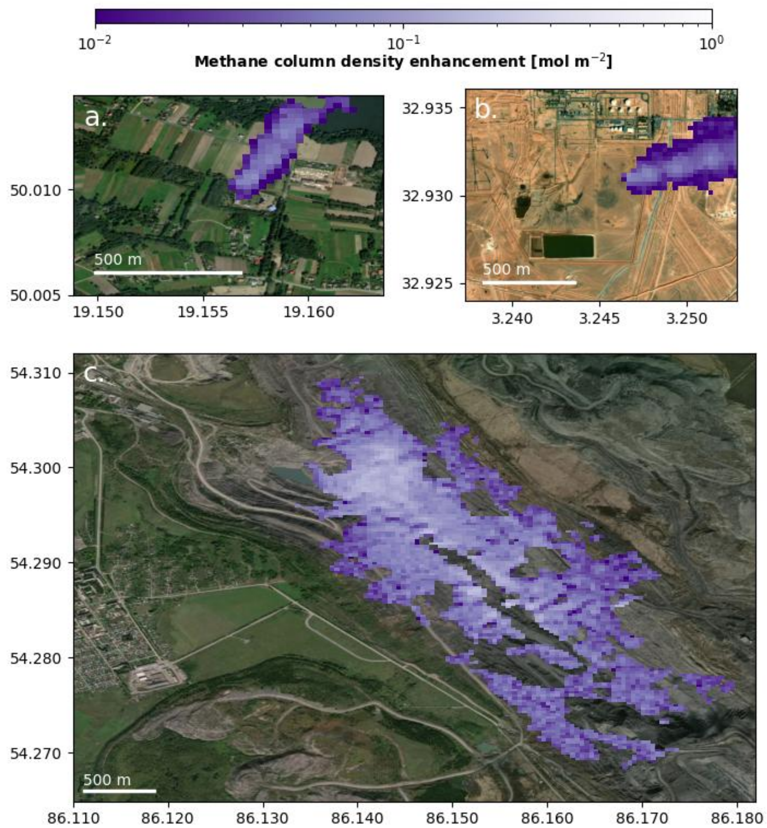


**Fig. 1.** Example GHGSat methane plume enhancements. Detected plumes from a a) coal vent, b) O&G flare stack, and c) open-pit coal mine.

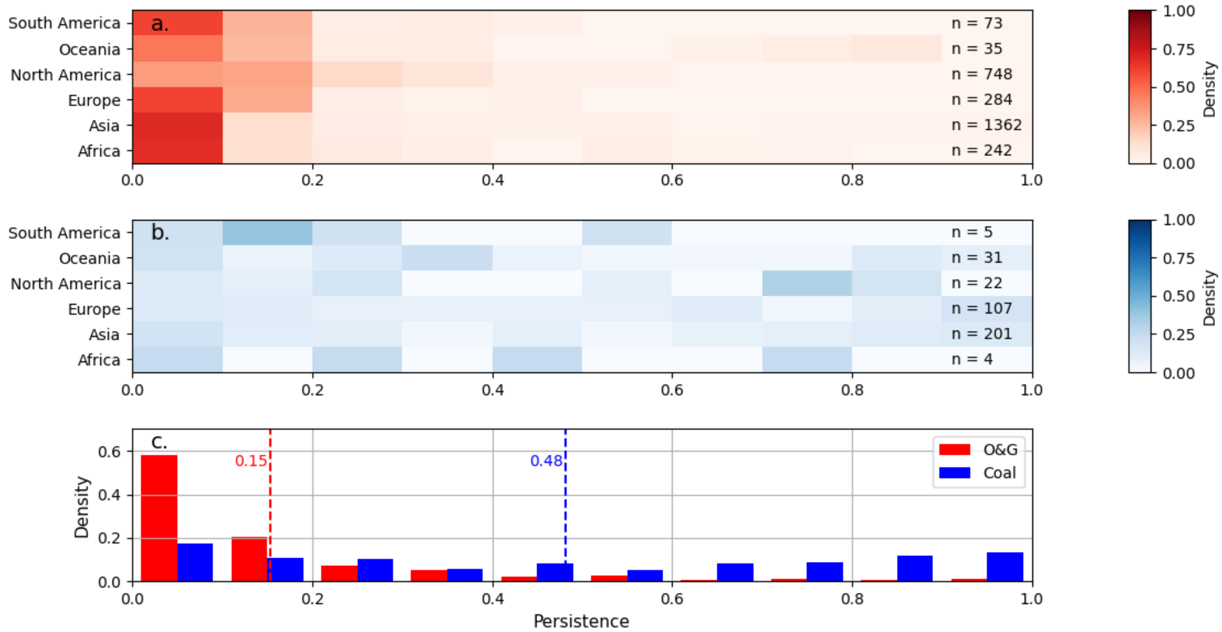


**Fig. 2.** Average site persistence distributions. a) Persistence distribution for O&G sites by continent with the number of sites $\boldsymbol{n}$ included in the average annotated. b) Persistence distribution for coal sites by continent. c) Persistence distributions for all O&G and coal sites. The average of the persistence distributions are indicated with the vertical dashed line: 0.15 for O&G sites and 0.48 for coal sites.

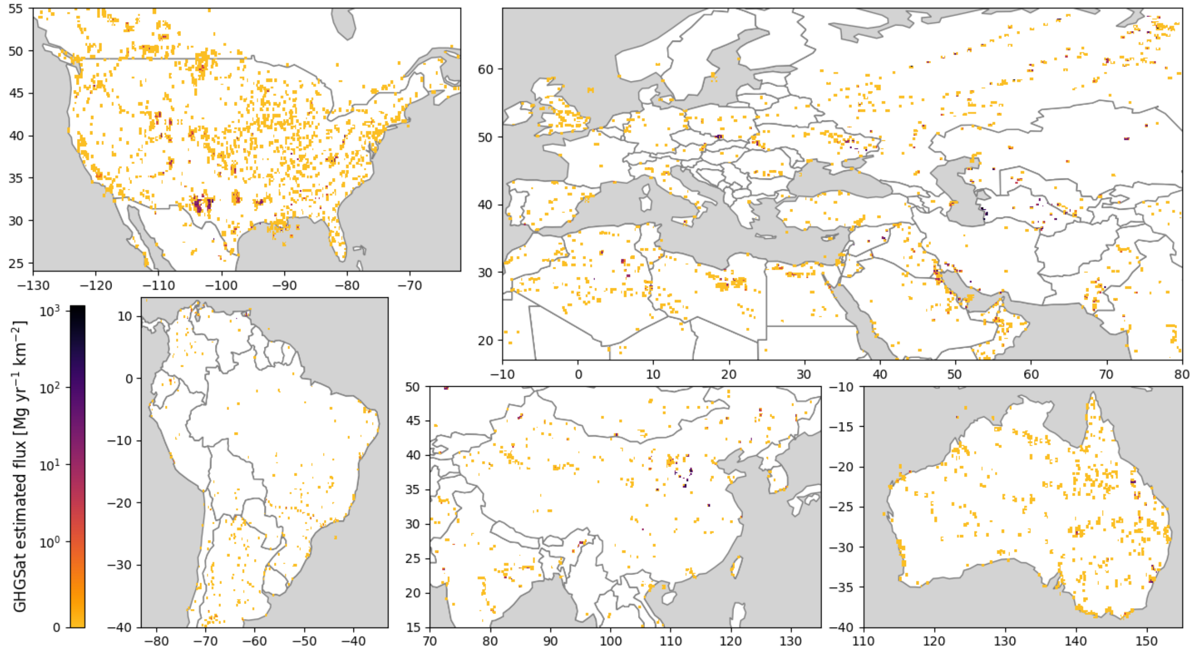


**Fig. 3.** Map of GHGSat estimated emissions. GHGSat estimated emission fluxes are shown at $\mathbf{0.2}^\circ$ x $\mathbf{0.2}^\circ$ resolution for selected regions around the globe. Each coloured area represents a location where GHGSat has made at least one clear-sky retrieval.

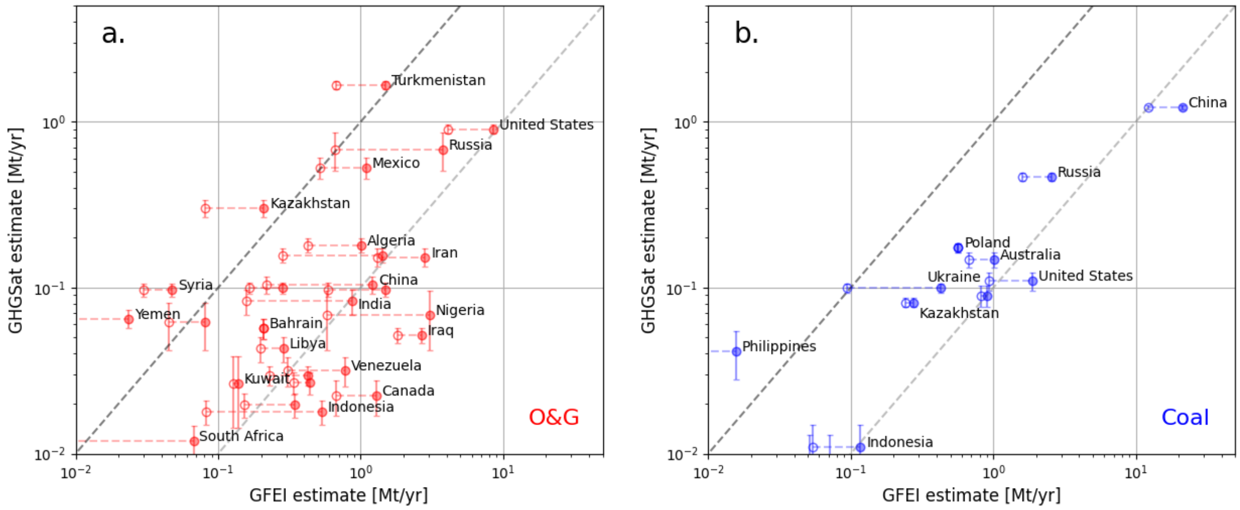


**Fig. 4.** Spatial correlation of emission estimates between GHGSat and GFEIv3. A comparison between GHGSat and GFEIv3 estimated emissions from O&G (Figure 4a) and coal (Figure 4b.) for countries. Solid points denote the GFEIv3 country total whereas open markers denote the GFEIv3 total for GHGSat-observed locations. Black dashed lines are the 1:1 lines, grey dashed lines show the 0.1:1 lines (i.e. where GHGSat emissions equal 10% of GFEI emissions).

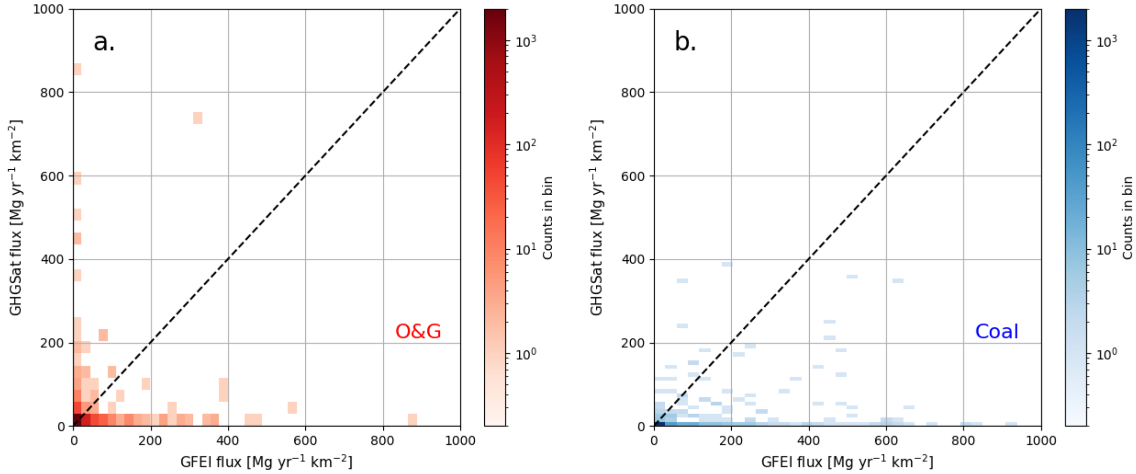


**Fig. 5.** Correlation between GHGSat and GFEIv3 flux estimates at $\mathbf{0.2}°$ x $\mathbf{0.2}°$ grid cell resolution for O&G (a.) and coal (b.). The black dashed line is the 1:1 line.

# Global Energy Sector Methane Emissions Estimated by using Facility-Level Satellite Observations

**Authors:** Dylan Jervis[1], Marianne Girard[1], Jean-Philippe W MacLean[1], David Marshall[1], Jason McKeever[1], Mathias Strupler[1], Antoine Ramier[1], Ewan Tarrant[1], David Young[1], Joannes D. Maasakkers[2], Ilse Aben[2], and Tia R. Scarpelli[3].

**Affiliations:**

[1]GHGSat Inc, Montreal, QC, Canada

[2]SRON Netherlands Institute for Space Research, Leiden, Netherlands

[3]Carbon Mapper, Pasadena, CA, USA

Corresponding author: dylan.jervis@ghgsat.com

## Materials and Methods

GHGSat Constellation

GHGSat launched its demonstration satellite, GHGSat-D in June 2016. Since then, it has launched 11 commercial methane satellites: GHGSat-C1 in September 2020, C2 in January 2021, C3-5 in May 2022, C6-C8 in April 2023, and C9 and C11 in November, 2023. All GHGSat satellites operate in the same way: solar backscattered radiation is measured by the instrument and the light is spectrally filtered using a Fabry-Perot optical cavity (*1*). The methane column density is estimated with 2.0% median precision (*2*) in targeted 15 x 12 – 15 x 30 $km^2$ retrieval domains with ~25 m spatial resolution. Plumes are identified in the column density field and a semi-automated masking procedure is applied before the source rate estimation is performed (*3*). The plume mask, source rate, time of detection, and estimated emission source location are stored, along with the retrieval footprint and other meta information. In the case where no plumes have been detected in the retrieval, the stored retrieval domain footprint can be used to identify locations that were observed to be not emitting.

The GHGSat constellation makes targeted observations of locations around the world. The targeting locations are chosen based on a combination of tip-and-cue information from TROPOMI (*4*), Sentinel-2 and Sentinel-3 detections (Varon et al., 2021),(*5*), information provided by ground operators or other associated personnel, commercial requests, time of year, weather forecast, among others.

The GHGSat measurements presented in this paper were taken during 2023. This is an extended time period over which GHGSat had increasing coverage capability with 8 commercial satellites in orbit: GHGSat-C1 (launched September 2020), C2 (launched January, 2021), C3/4/5 (launched May 2022), C6/7/8 (launched April 2023). The data presented here is the result of 97.7% of our 2023 O&G and coal catalogue. Summary details of GHGSat observations and detections are presented in Table S1. No commercial partners had any advance notice or input regarding the analysis presented in this paper.

Spatial Aggregation of Detections and Null Observations

In order to attribute plumes with ambiguous origin points to common source locations, we perform a spatial aggregation procedure whereby any plume within a specified distance from another plume is attributed to the same source location. We choose the aggregation distance to be 300m for O&G and 2km for coal. The result is a cluster of $M_i$ plumes that have been attributed to site $i$. A visual example of how plumes are aggregated into sites is seen in Figure S1 for an example region.

The choice of plume aggregation distance will affect 1) estimated site emission rate, 2) the number of distinct sites, and 3) the persistence. In Figure S2, we vary the aggregation distance for both the O&G and coal sector to see how these three quantities change. For both sectors, increasing the aggregation distance reduces the number of distinct sites and increase the average estimated persistence. This is intuitive since the larger the aggregation distance, the more plumes aggregated into a common site. The more plumes are aggregated into a common site, the greater the persistence since the number of null observations as very insensitive to the aggregation distance. The total estimated emissions is not especially sensitive to a change in the aggregation distance: changing only ~5% for O&G when the aggregation distance is changed from 100m to 500m , and only ~15% for coal when the distance is changed from 500m to 3000m. For the results presented in this study, we chose an aggregation distance of 300 m for O&G and 2 km for coal.

Estimated Persistence

After the $M_i$ detected plumes have been have spatially aggregated for site $i$, the number of "null" detection events for that site are counted – i.e. the number of times each site was successfully observed (i.e. a clear-sky observation where a retrieval was successfully performed) without a plume being detected. This is done using knowledge of the retrieval measurement footprint and a procedure that checks whether site $i$ was located inside of it. The inclusion of the null observations results in $N_i$ total observations for site $i$. With these $N_i \geq M_i$ total observations, we can estimate the average emission rate of each site:

$$\hat{Q}_i = Q_{q\neq 0;i} \cdot \langle \hat{p} \rangle_i \tag{1}$$

where

$$Q_{q\neq 0;i} = \frac{\sum_{j=1}^{M_i} q_{q\neq 0;i;j}}{M_i} \tag{2}$$

is the average of the $M_i$ non-zero emission rates $q_{q\neq 0;i;j}$ with the $j$ index counting the observations taken at different times for site $i$. Null measurements (i.e. when $q_{i;j} = 0$) are included via the estimated site persistence:

$$\langle \hat{p} \rangle_i = \int_0^1 x \hat{p}_i(x)\, dx. \tag{4}$$

The estimated site persistence $\langle \hat{p} \rangle_i$ is the mean of the posterior persistence distribution $\hat{p}_i(x)$ which is, in turn, calculated from a prior persistence distribution $p_p(x)$ and the observed site probability distribution $p_i(x)$:

$$\hat{p}_i(x) = p_p(x) p_i(x). \tag{5}$$

The observed site probability distribution is modelled as a binomial distribution:

$$p_i(x) = x^{M_i}(1-x)^{N_i - M_i} \tag{6}$$

With $x$ being the persistence variable and the mean of this distribution being the observed site persistence $\langle p \rangle_i = M_i/N_i$. The prior probability distributions are constructed on a continent and sector-specific basis from sites that have had at least 10 observations. If there are fewer than 10 sites for a given continent and sector then the global average persistence distribution for a particular sector is used. The prior persistence distributions are shown in section S6.

For sites with a large number $N_i$ of observations, the observed site probability distribution $p_i(x)$ becomes sharply peaked around $\langle p \rangle_i$, implying $\langle \hat{p} \rangle_i \approx M_i/N_i$. Conversely, when there are only a few observations at a site, the observed site probability distribution $p_i(x)$ becomes quite broad and the prior probability distribution has more influence on the estimated site persistence $\langle \hat{p} \rangle_i$ .

Figure S3 presents an illustration of how the estimated site persistence is calculated. Imagine we have a prior persistence distribution $p_p(x)$ (red bars) with a mean of 0.16. In this example, a site from the same sector and continent is measured either $N = 3$ or 90 times, with the same observed persistence of 0.33 (i.e. $M$=1 or 30, respectively). The binomial distribution $p_i(x) = x^M(1-x)^{N-M}$ for both cases are peaked at 0.33, but the $N$=90 case (black line) is more sharply peaked than the $N$=3 case (grey line). This results in an estimated persistence $\langle \hat{p} \rangle$ that is much closer to $M/N$ for the $N$=90 case ($\langle \hat{p} \rangle$=0.29) than for the $N$=3 case ($\langle \hat{p} \rangle$=0.19).

We estimate an error $\delta\hat{Q}_i$ for the site emission rate as having contributions from both the weighted error of the mean of the detected emission rates $\delta Q_{e;i}$ and the sampling error $\delta Q_{s;i}$:

$$\delta\hat{Q}_i = \sqrt{\delta Q_{e;i}^2 + \delta Q_{s;i}^2}. \quad (7)$$

The smaller the source rate error on individual emissions, the smaller $\delta Q_{e;i}$ will be. The more observations for a given site, the smaller $\delta Q_{s;i}$ will be. The error contribution from the individual source rate error is:

$$\delta Q_{e;i} = \frac{\hat{Q}_i}{\sqrt{\sum_j^{M_i} w_{i;j}}} \quad (8)$$

with the weights defined as the inverse of the fractional variance of each measurement:

$$w_{i;j} = \frac{1}{\left(\delta q_{q\neq 0;i;j}/q_{q\neq 0;i;j}\right)^2} \quad (9)$$

where $\delta q_{q\neq 0;i;j}$ is the emission rate error. The error contribution from finite sampling statistics is:

$$\delta Q_{s;i} = \hat{Q}_i \sqrt{\frac{1-\langle p\rangle_i}{\langle p\rangle_i N_i}}. \quad (10)$$

The total emissions estimate for a given region is the sum of the $k$ individual average site emission rates in that region:

$$\hat{Q}_{tot} = \sum_{i=1}^{k} \hat{Q}_i \quad (11)$$

with the total error being equal to the sum of the site errors in quadrature:

$$\delta\hat{Q}_{tot} = \sqrt{\sum_{i=1}^{k} \left(\delta\hat{Q}_i\right)^2}. \quad (12)$$

It is important to note that our site emission rate estimate relies on an ergodic assumption about our measurement sample. We assume that our measurements are capturing representative and unbiased snapshots of the site's dynamical emission rate behaviour from which we infer an average rate. This assumption may be broken due to a number of features of our observation system. First is the fact that our satellite instruments can only make measurements during daylight hours (usually between 10am – 2pm local time), which may be correlated (or anti-correlated) with the timing of facility operations that affect emissions. Second, our current ~1 week revisit period may be incommensurate with the duration of certain emission events. This could, for instance, lead to an overestimate of emissions for sites with emission events lasting ~1hr when a plume was detected (and then implicitly assumed to be emitting for the average revisit period of that site) and miss emission events entirely for other similarly emitting sites when the satellite overpass was not coincident with emission events.

We can derive a mathematical framework for how correlated errors could be included, should we gain knowledge about these in the future. Let us say that for site $i$ our error estimate $\delta\hat{Q}_i$ has not only a random component $\delta\hat{Q}_{i;r}$ defined by Equation 7, but also a correlated component $\delta\hat{Q}_{i;c}$, and that these can be added in quadrature (since the random and correlated errors are not themselves correlated):

$$\delta\hat{Q}_i = \sqrt{\left(\delta\hat{Q}_{i;r}\right)^2 + \left(\delta\hat{Q}_{i;c}\right)^2} \tag{13}$$

The total error is then

$$\delta\hat{Q}_{tot} = \sqrt{\left(\delta\hat{Q}_{tot;r}\right)^2 + \left(\delta\hat{Q}_{tot;c}\right)^2} \tag{14}$$

With the total random error being added in quadrature:

$$\delta\hat{Q}_{tot;r} = \sqrt{\sum_{i=1}^{k}\left(\delta\hat{Q}_{i;r}\right)^2} \tag{15}$$

And the correlated error added linearly:

$$\delta\hat{Q}_{tot;c} = \sum_{i=1}^{k}\delta\hat{Q}_{i;c} \tag{16}$$

It is also important to acknowledge that our spatial aggregation method assumes that all emissions emanate from distinct methane sources. For the real-world cases where this assumption is broken, say for two far-apart plumes from a distributed source such as a pipeline, the method described here will count those plumes as coming from two separate sources with half the persistence of the actual emissions. But the total emission estimate from the two sources combined would be similar, up to the effect that the prior persistence distribution has on the estimate.

Correlation Coefficient

The standard Pearson correlation coefficient between two vectors $x$ and $y$ is defined as

$$r = \frac{\mathrm{Cov}(x,y)}{\sqrt{\mathrm{Var}(x)\mathrm{Var}(y)}} \tag{17}$$

With the covariance defined as

$$\mathrm{Cov}(x,y) = \sum_i (x_i - \bar{x})(y_i - \bar{y}) \tag{18}$$

And the variance defined as

$$\mathrm{Var}(x) = \sum_i (x_i - \bar{x})^2 \tag{19}$$

With $\bar{x}$ being the mean of vector $x$, and likewise for $y$.

In the case where we have an error vector $\sigma_y$ associated with the vector $y$, for example the GHGSat emissions estimate, we may calculate and error-weighted correlation coefficient $r$. We can still use the expression above to calculate $r$, but with the following substitutions for the covariance:

$$\mathrm{Cov}(x, y) = \frac{\sum_i w_i (x_i - \bar{x})(y_i - \bar{y}_w)}{\sum_i w_i} \tag{20}$$

With the weights $w_i$ defined as the variance-normalized value to balance the significance and reliability of the estimates

$$w_i = \frac{y_i}{\sigma_{y;i}^2}. \tag{21}$$

The variance $\mathrm{Var}(y)$ calculated as

$$\mathrm{Var}(y) = \frac{\sum_i w_i (y_i - \bar{y}_w)^2}{\sum_i w_i} \tag{22}$$

with the weighted mean $\bar{y}_w$ calculated as

$$\bar{y}_w = \frac{\sum_i w_i y_i}{\sum_i w_i}. \tag{23}$$

GFEIv3

The Global Fuel Exploitation Inventory version 3 (GFEIv3) is a spatially gridded inventory that is constructed by disaggregating the nationally reported 2010-2020 UNFCCC methane emissions in the O&G and coal sectors to $0.1°$x $0.1°$ resolution using knowledge of infrastructure locations within each country (*6*). GFEIv3 is an update of the GFEIv2 (*7*) and GFEIv1 (*8*). The GFEIv3 data is provided as a netCDF file with the GFEIv3 O&G emissions data used in our analysis defined to be the sum of the 'Oil_All' and 'Gas_All' data variables, and the GFEIv3 coal emissions data given by the 'Coal' data variable. GFEIv3 emissions data is provided in units of flux (Mg $yr^{-1}$ $km^{-2}$). It is binned to $0.2°$x $0.2°$ resolution by taking the mean flux value over the four $0.1°$x $0.1°$ grid cells that comprise the binned grid cell and converted to an emission rate by multiplying by the area encompassed by that grid cell at its specific latitude and longitude.

**Supplementary Text:**

**S1 Plume Map**

The O&G and coal plumes detected by GHGSat in 2023 are shown in Figure S4. These plumes - in combination with null observations - are used to estimate spatially gridded fluxes. In many locations, large plumes obscure the presence of smaller plumes. In total, there were 11,419 plumes detected by GHGSat in 2023 from the O&G + coal sectors.

**S2 Site observation details**

The distributions of the number of observations per emitting site in 2023 is shown In Figure S5.

**S3 Prior Persistence Distribution**

The prior persistence distribution for each continent and sector is shown in Figure S6. This prior distribution is used to estimate the persistence for all sites and is especially important in accurately estimating the persistence and average emission rate for sites that have been observed only a handful of times. The prior persistence distribution only includes sites where we have made at least 10 observations. To use a continent-specific prior distribution for a given sector, we require there to be at least 10 observations. Otherwise, the globally-averaged distribution for a given sector is used.

**S4 Temporal Autocorrelation of Observations and Detections**

We investigate the temporal distribution of observations and detections using an autocorrelation function. The probability of observing a site, or detecting an emission, a time $t+\tau$ after previously observing a site, or detecting an emission, at time $t$ at site $i$ is given by the conditional probability:

$$P_i(1 \text{ at } t+\tau | 1 \text{ at } t) = \frac{R_i(\tau)}{R_i(0)} \tag{24}$$

Where $R_u(\tau)$ is the uncentered autocorrelation function:

$$R_i(\tau) = \frac{\sum_i^k d_i(t)\, d_i(t-\tau_j)}{k} \tag{25}$$

And $d_i(t)$ is the either the observation vector (equal to 1 at time $t$ if the site was observed, and 0 if not) or the detection vector (equal to 1 at time $t$ if an emission was detected, 0 if the site was observed without detecting an emission, and not assigned any value if the site was not observed at the time). We discretize time into days – i.e. each subsequent element in the detection vector is separated by one day ($t_{i+1} - t_i = 1$ day) – and so $k$=365, the number of days in the observation period presented in this paper.

In Figure S7, we plot the average of $P_i(1 \text{ at } t+\tau | 1 \text{ at } t)$ over $N$ sites:

$$\langle P(\tau) \rangle = \frac{1}{N} \sum_i^N P_i(1 \text{ at } t+\tau | 1 \text{ at } t) \tag{26}$$

For the case of the conditional detection probability where the vector $d(\tau)$ can have an unassigned value (i.e. NaN), we only report an average value $\langle P(\tau)\rangle$ at delay time $\tau$ if there are at least 2 assigned values – whether they be 1 or 0 – used in the average.

The probability of an observation is equal to 1 at $\tau = 0$ by definition. It immediately decays to values near ~5% - i.e. close to the average revisit frequency given the 18-day average revisit time. A constant temporal probability value for $\tau > 0$ is indicative of a random distribution of observation times. While our observation probability is relatively flat for all $\tau$, it slowly decays from 7% at $\tau < 7$ days to 3% for $\tau > 300$ days. That is, we make slightly more observations of a site for shorter revisit times versus for longer ones.

The temporal detection probability for O&G and coal sites is noisier than the temporal observation probability because the detection vector only has values assigned during observation times. Nevertheless, we can observe that the temporal detection probability immediately decays from 1 at $\tau = 0$ to a value close to the respective sector's average site persistence for $\tau > 0$. This is indicative of a emission detection pattern that is mostly random in time. The $\langle P(\tau > 0)\rangle$ value isn't exactly equal to the average estimated persistence value because we are calculating the temporal detection probability from a detection vector that doesn't use information from the prior persistence distribution. Regardless, Figure S7 shows that we are more likely to observe an emission from an O&G site a short time (~weeks) after previously observing an emission. The situation for coal detections is a little more ambiguous due to the increased noise in the temporal probability of detection (due to there being not as many coal sites included in the average). With more coverage in the future, we will hopefully be able to tease out more information about the temporal behaviour of these sources.

## S5 Number of Observations

The number of 2023 clear-sky GHGSat observations within each $0.2° \, x \, 0.2°$ grid cell is shown in Figure S8.

## S6 Map of Difference between GHGSat and GFEI estimated emissions

The difference between GHGSat and GFEIv3 estimated emissions within each $\mathbf{0.2}° \, \boldsymbol{x} \, \mathbf{0.2}°$ grid cell is shown in Figure S9.

## S7 National O&G + Coal Emission Rates Estimated by GHGSat

In Figure S10 and Table S2, we compare emissions between GHGSat and GFEIv3 at the country level. Country level emission estimates are presented in Figure S10a for the top 15 emitting countries as measured by GHGSat (the complete country-level estimated measured by GHGSat are presented in the table below). Figure S11a shows the sector-resolved GHGSat measured emission rates for each country (O&G in red, coal in blue) with the fraction of total GFEIv3 emissions that the combined O&G + coal total represents quantified in the annotation. GHGSat measured a sizeable fraction of nationally reported energy emissions for certain countries**:** 111% of reported O&G + coal emissions in Turkmenistan, 18% in Russia, 79% in Kazakhstan, 19% in Australia, and 27% in Poland, etc.. Given that the GHGSat constellation is only able to observe a portion of actual emissions due to its imperfect detection threshold and coverage, many of these nationally reported emission totals are likely to be underestimated, consistent with previous studies (*9*, *10*). We show in Figure S10b the observational coverage fraction that GHGSat has achieved in each country. We quantify GHGSat coverage as the GFEIv3 emission flux-weighted fraction of grid cells observed by GHGSat at least once:

$$C_F = \frac{\sum_i c_i f_i}{\sum_i f_i} \tag{27}$$

Where $c_i$ is equal to 1 at grid cell $i$ if GHGSat has observed it at least once and 0 otherwise, and $f_i$ is the GFEIv3 flux. If the flux $f_i$ was constant everywhere, then $C_F$ would represent the area coverage. We see that the GHGSat constellation observes areas accounting for between 5% and 100% in these selected high-emitting countries.

## S8 Comparison of GHGSat and GFEI estimates for selected countries

In Figures S11-S15, we provide a comparison of GHGSat emission estimates with those of GFEIv3 for selected countries and sectors (Mexico O&G, Iraq O&G, Poland Coal mining, Australia Coal mining, and Turkmenistan O&G). For some selected countries and sectors, the GHGSat estimate is similar to the GFEIv3 estimate when aggregating grid cells within the country that GHGSat has observed (e.g. Mexico O&G); for some countries the GHGSat estimate is higher (e.g. Turkmenistan O&G), for other countries the estimate is moderately lower (e.g. Poland and Australia Coal mining), and for some countries the GHGSat estimate is substantially lower (e.g. Iraq O&G). In each plot panel the GHGSat emission estimate is shown for each observed 0.2 x 0.2 degree grid cell alongside an error estimate for grid cells with a nonzero emission estimate. Also shown are the GFEI estimates at the grid cells observed by GHGSat at least once, as well as all GFEI grid cell estimates within the country with at least 1 Mg $yr^{-1}$ $km^{-2}$.

## References

1. D. Jervis, J. McKeever, B. O. A. Durak, J. J. Sloan, D. Gains, D. J. Varon, A. Ramier, M. Strupler, E. Tarrant, The GHGSat-D imaging spectrometer. *Atmos Meas Tech* **14**, 2127–2140 (2021).
2. A. Ramier, M. Girard, D. Jervis, J.-P. Maclean, D. Marshall, J. Mckeever, M. Strupler, E. Tarrant, D. Young, “High-Resolution Methane Detection with the GHGSat Constellation” (2023).
3. D. J. Varon, D. J. Jacob, J. McKeever, D. Jervis, B. O. A. Durak, Y. Xia, Y. Huang, Quantifying methane point sources from fine-scale satellite observations of atmospheric methane plumes. *Atmos Meas Tech* **11**, 5673–5686 (2018).
4. B. J. Schuit, J. D. Maasakkers, P. Bijl, G. Mahapatra, A. W. Van Den Berg, S. Pandey, A. Lorente, T. Borsdorff, S. Houweling, D. J. Varon, J. McKeever, D. Jervis, M. Girard, I. Irakulis-Loitxate, J. Gorroño, L. Guanter, D. H. Cusworth, I. Aben, Automated detection and monitoring of methane super-emitters using satellite data. *Atmos Chem Phys* **23**, 9071–9098 (2023).

5. D. J. Varon, D. Jervis, J. McKeever, I. Spence, D. Gains, D. J. Jacob, High-frequency monitoring of anomalous methane point sources with multispectral Sentinel-2 satellite observations. *Atmos Meas Tech* **14**, 2771–2785 (2021).
6. T. R. Scarpelli, E. Roy, D. J. Jacob, M. P. Sulprizio, R. D. Tate, D. H. Cusworth, Using new geospatial data and 2020 fossil fuel methane emissions for the Global Fuel Exploitation Inventory (GFEI) v3. doi: 10.7910/DVN/HH4EUM.
7. T. R. Scarpelli, D. J. Jacob, S. Grossman, X. Lu, Z. Qu, M. P. Sulprizio, Y. Zhang, F. Reuland, D. Gordon, J. R. Worden, Updated Global Fuel Exploitation Inventory (GFEI) for methane emissions from the oil, gas, and coal sectors: Evaluation with inversions of atmospheric methane observations. *Atmos Chem Phys* **22**, 3235–3249 (2022).
8. T. R. Scarpelli, D. J. Jacob, J. D. Maasakkers, M. P. Sulprizio, J. X. Sheng, K. Rose, L. Romeo, J. R. Worden, G. Janssens-Maenhout, A global gridded (0.1° × 0.1°) inventory of methane emissions from oil, gas, and coal exploitation based on national reports to the United Nations Framework Convention on Climate Change. *Earth Syst Sci Data* **12**, 563–575 (2020).
9. L. Shen, D. J. Jacob, R. Gautam, M. Omara, T. R. Scarpelli, A. Lorente, D. Zavala-Araiza, X. Lu, Z. Chen, J. Lin, National quantifications of methane emissions from fuel exploitation using high resolution inversions of satellite observations. *Nat Commun* **14**, 4948 (2023).
10. T. Lauvaux, C. Giron, M. Mazzolini, A. D'aspremont, R. Duren, D. Cusworth, "Global assessment of oil and gas methane ultra-emitters."

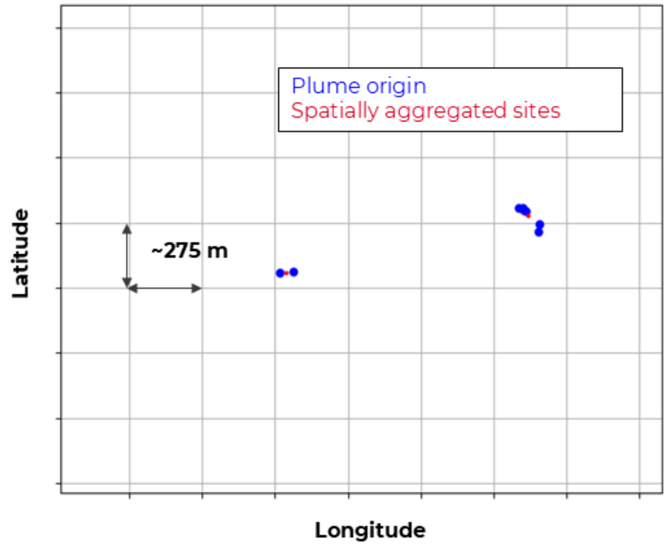


**Fig. S1:** Example of plume aggregation procedure.

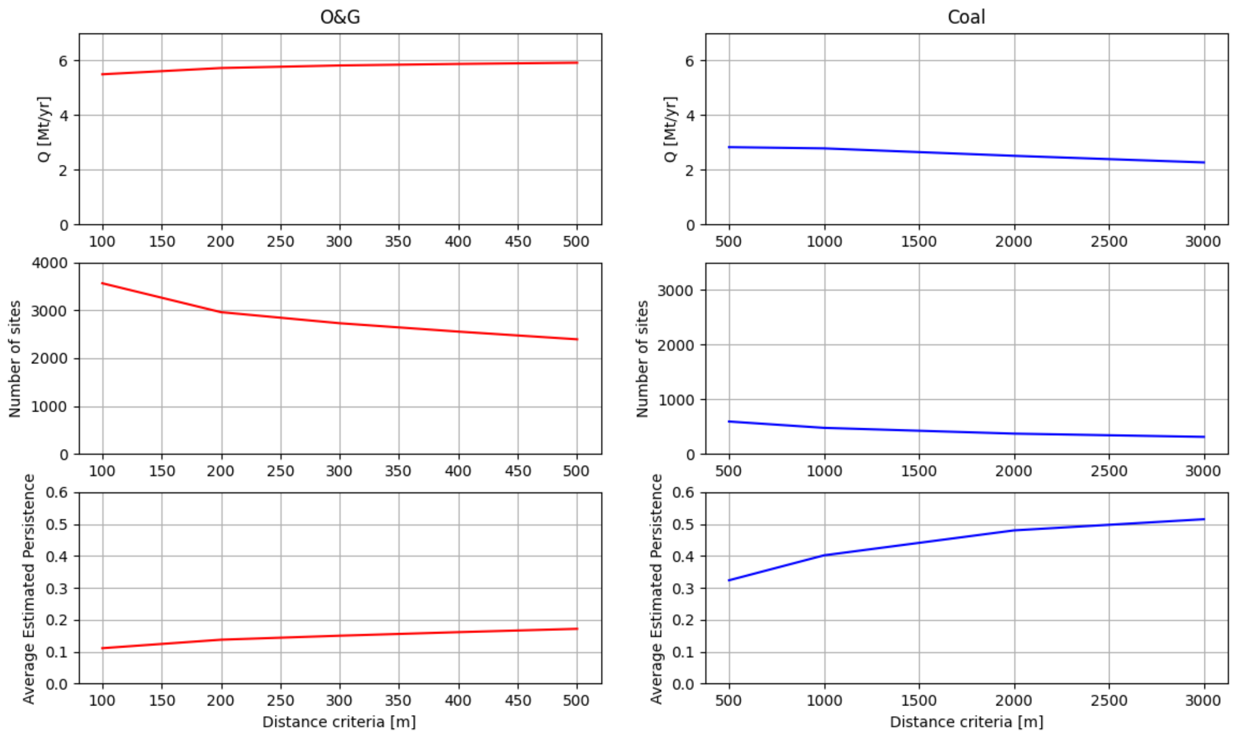


**Fig. S2:** Dependence of total emission estimates, number of unique sites, and average persistence on the spatial aggregation radius. We choose a spatial aggregation distance of 300m for O&G and 2km for coal.

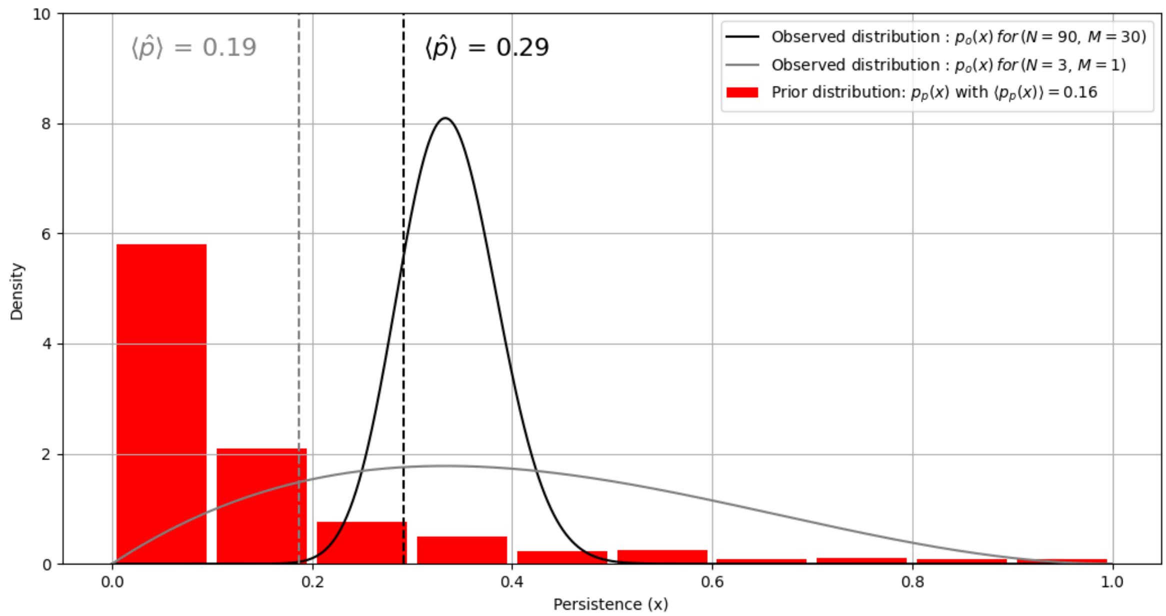


**Fig. S3**: Persistence estimation illustration. The red bars denote the prior distribution $\boldsymbol{p_p(x)}$ with mean 0.16. The black line is the Bernoulli distribution $\boldsymbol{p_o(x)}$ for $(\boldsymbol{N}, \boldsymbol{M}) = (\mathbf{90}, \mathbf{30})$, and the grey solid lines is the distribution for $(\boldsymbol{N}, \boldsymbol{M}) = (\mathbf{3}, \mathbf{1})$. Both cases have the same mean "observed" persistence $\boldsymbol{M/N}$=0.33. The dashed black and grey lines show the estimated persistence values $\langle\widehat{\boldsymbol{p}}\rangle$ for the $\boldsymbol{N}$=90 and 3 cases, respectively.

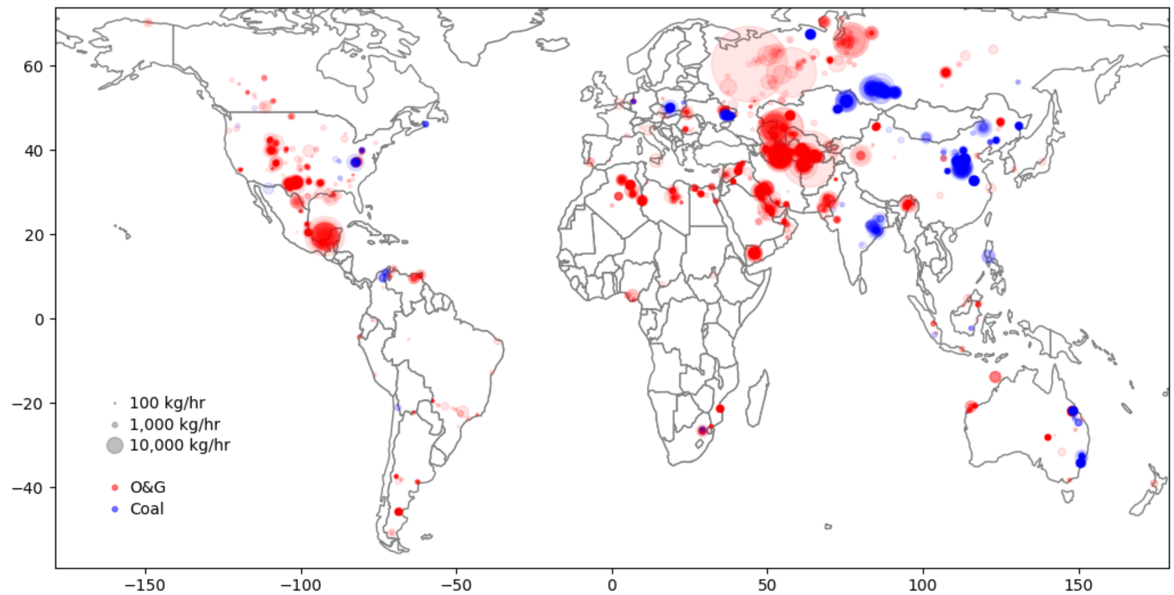


**Fig. S4:** Location and emission rates of the11,419 O&G + coal plumes observed in 2023 by GHGSat.

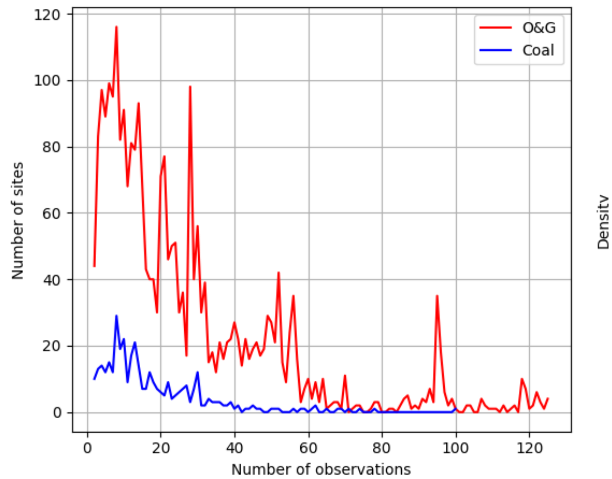


**Fig. S5:** Distribution of the number of GHGSat observations per emitting site in 2023.

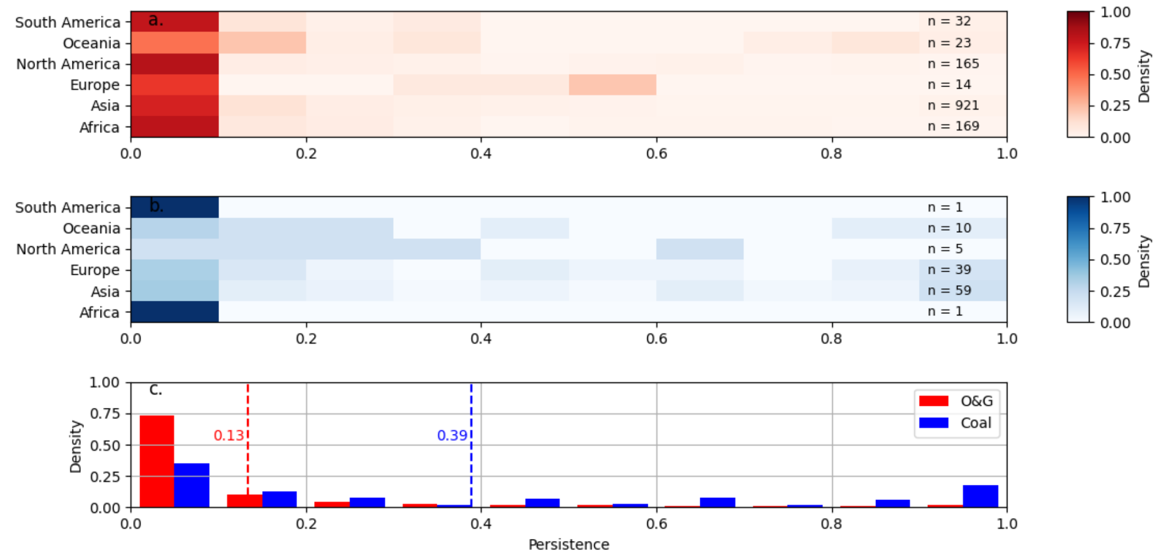


**Fig. S6:** Prior persistence distribution for O&G (top) and coal (middle) broken down by continent with the number of sites $\boldsymbol{n}$ included in the distribution annotated. The persistence distribution of all sites within either the O&G or coal sector are shown at bottom.

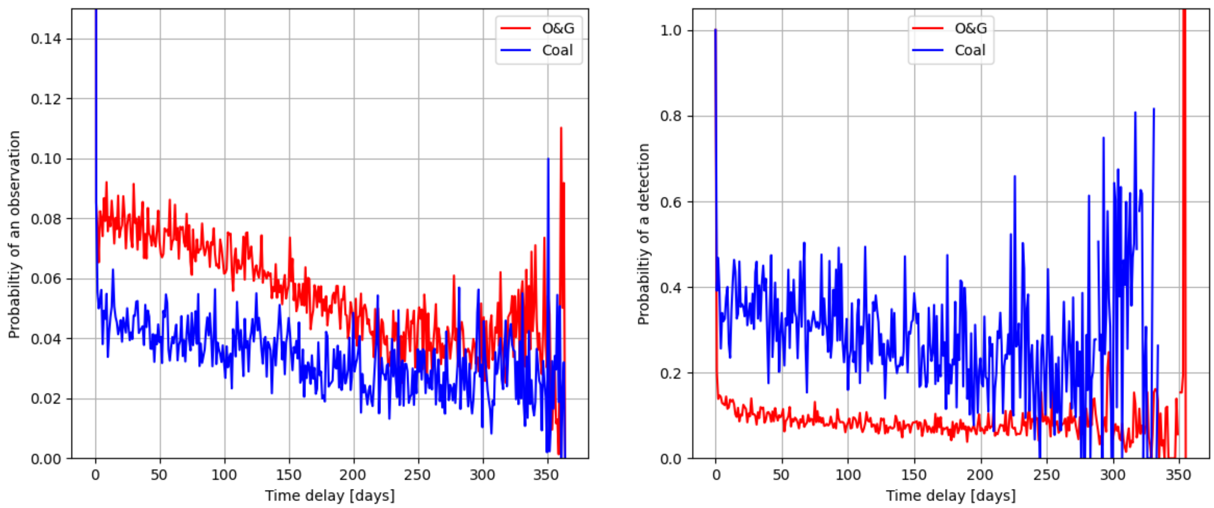


**Fig. S7:** Probability of observing a site (left) and detecting an emission (right) some time $\boldsymbol{\tau}$ after previously observing a site or detecting an emission.

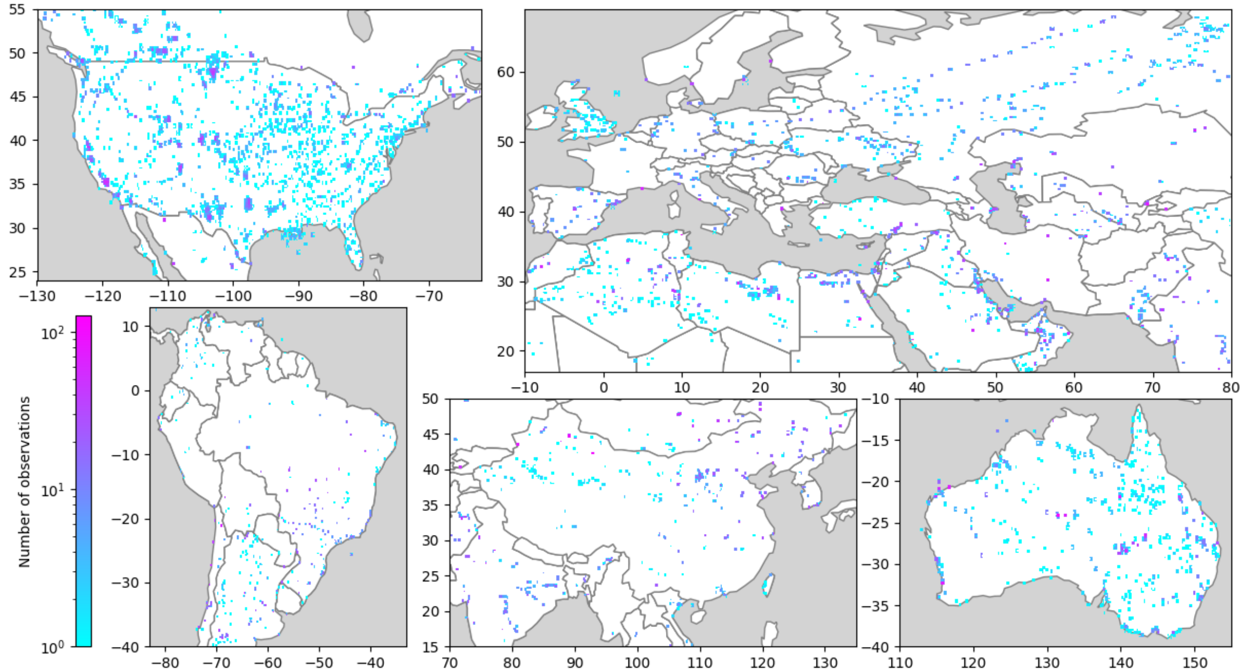


**Fig. S8:** The number of clear-sky observations taken by GHGSat per $\mathbf{0.2^\circ}\ \boldsymbol{x}\ \mathbf{0.2^\circ}$grid cell in 2023.

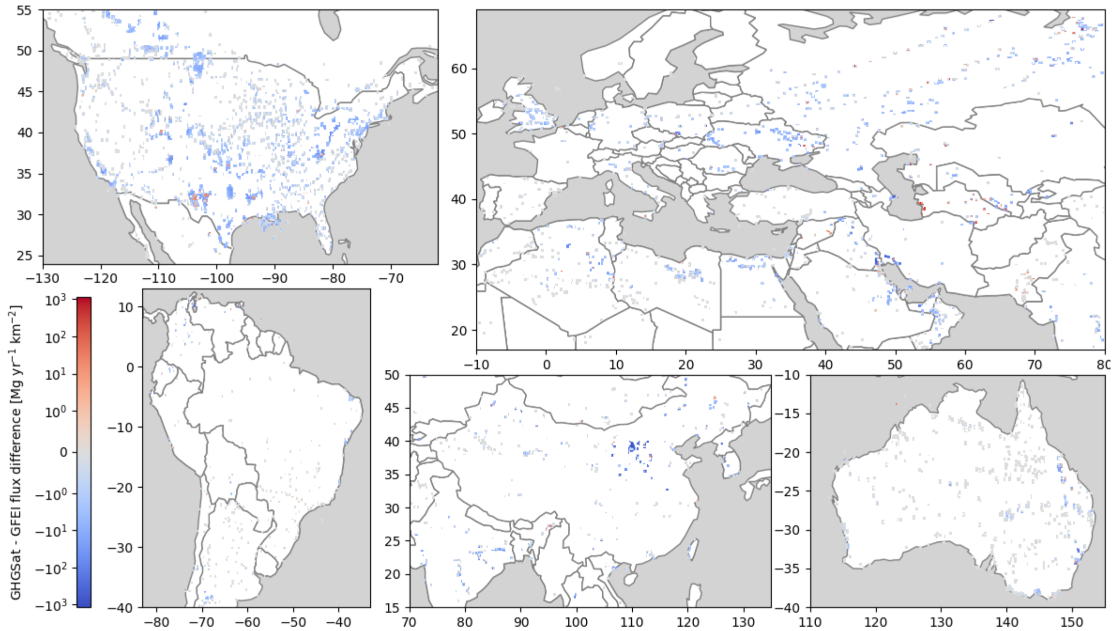


**Fig. S9:** The difference between GHGSat and GFEIv3 estimated emission flux in each $\mathbf{0.2^{\circ}}\ \boldsymbol{x}\ \mathbf{0.2^{\circ}}$ grid cell in 2023.

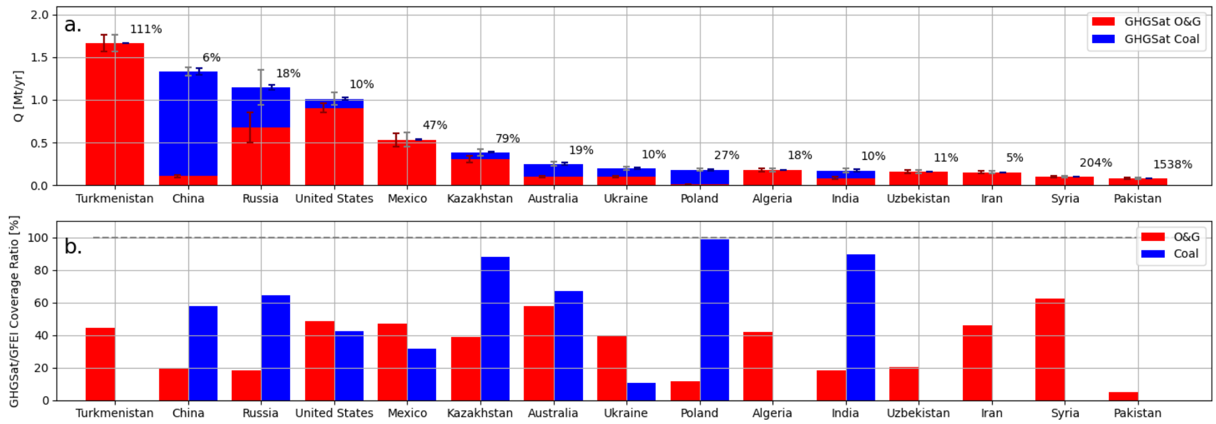


**Fig. S10.** National GHGSat emission estimates. Country-level O&G + coal emission estimates for the top-15 emitting countries (as measured by GHGSat). a) GHGSat estimated emissions (with percentage of total O&G + coal GFEIv3 emissions indicated in annotation). b) GHGSat observation coverage of GFEIv3 grid cells.

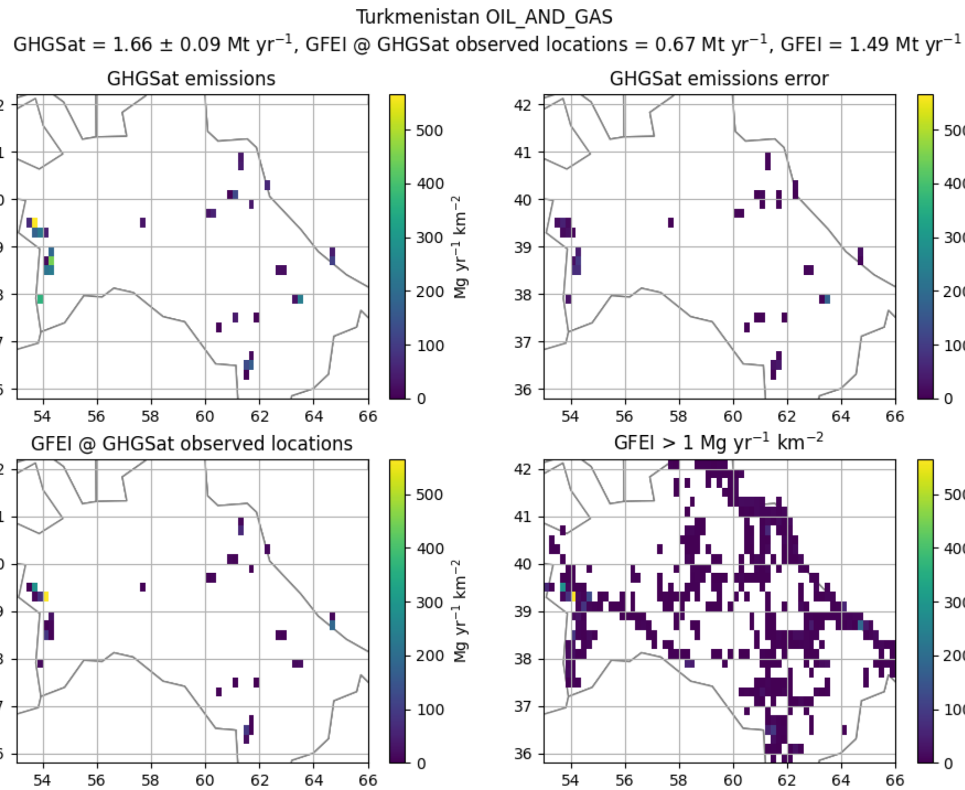


**Fig. S11.** Gridded GHGSat emissions (top left), GHGSat emissions error (top right), GFEIv3 emissions estimate at GHGSat-observed locations (bottom left), and GFEIv3 emissions (bottom right) for the case of Turkmenistan's O&G sector.

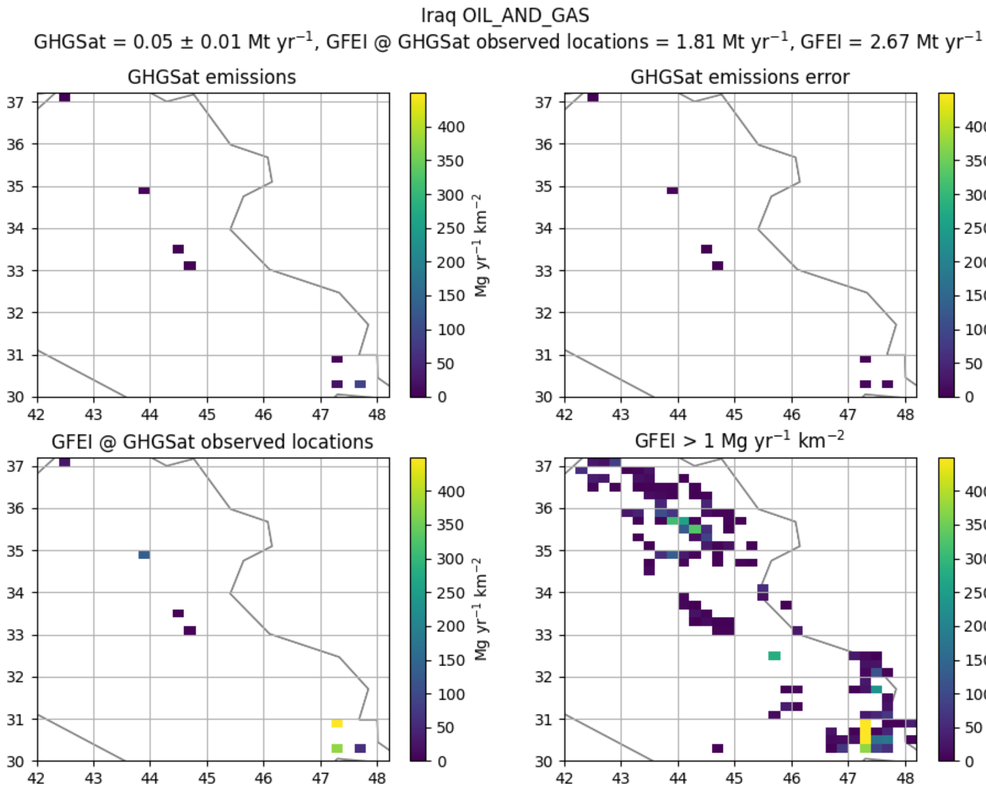


**Fig. S12.** Gridded GHGSat emissions (top left), GHGSat emissions error (top right), GFEIv3 emissions estimate at GHGSat-observed locations (bottom left), and GFEIv3 emissions (bottom right) for the case of Iraq's O&G sector.

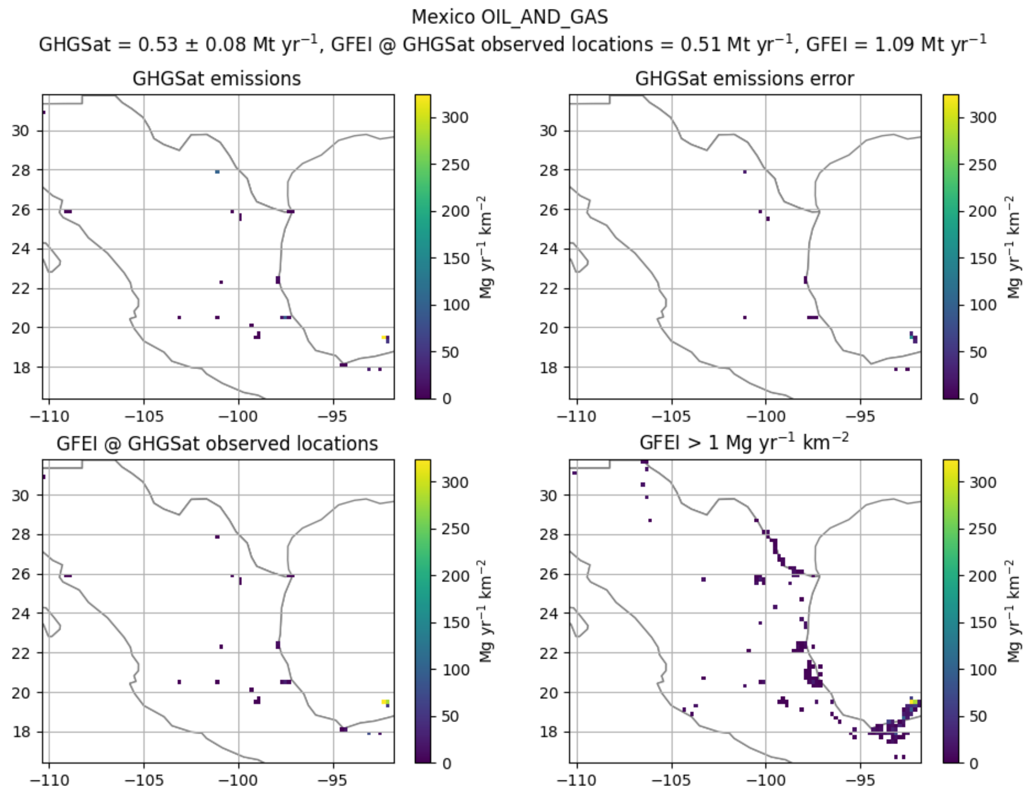


**Fig. S13.** Gridded GHGSat emissions (top left), GHGSat emissions error (top right), GFEIv3 emissions estimate at GHGSat-observed locations (bottom left), and GFEIv3 emissions (bottom right) for the case of Mexico's O&G sector.

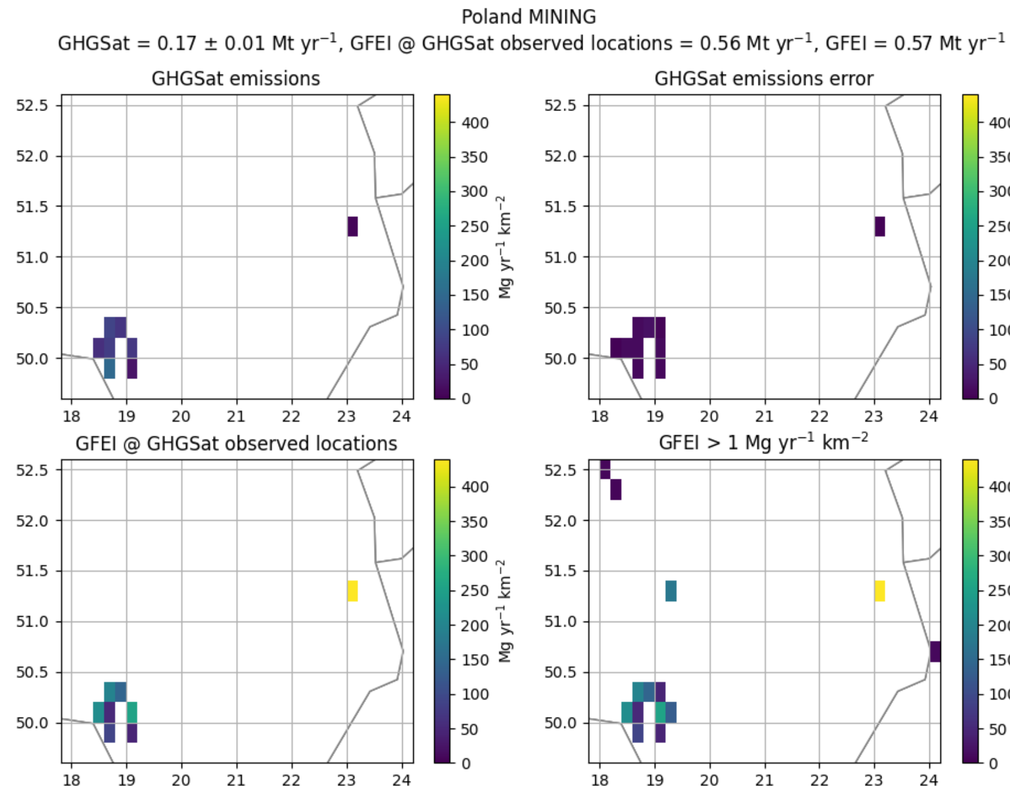


**Fig. S14.** Gridded GHGSat emissions (top left), GHGSat emissions error (top right), GFEIv3 emissions estimate at GHGSat-observed locations (bottom left), and GFEIv3 emissions (bottom right) for the case of Polands's Coal sector.

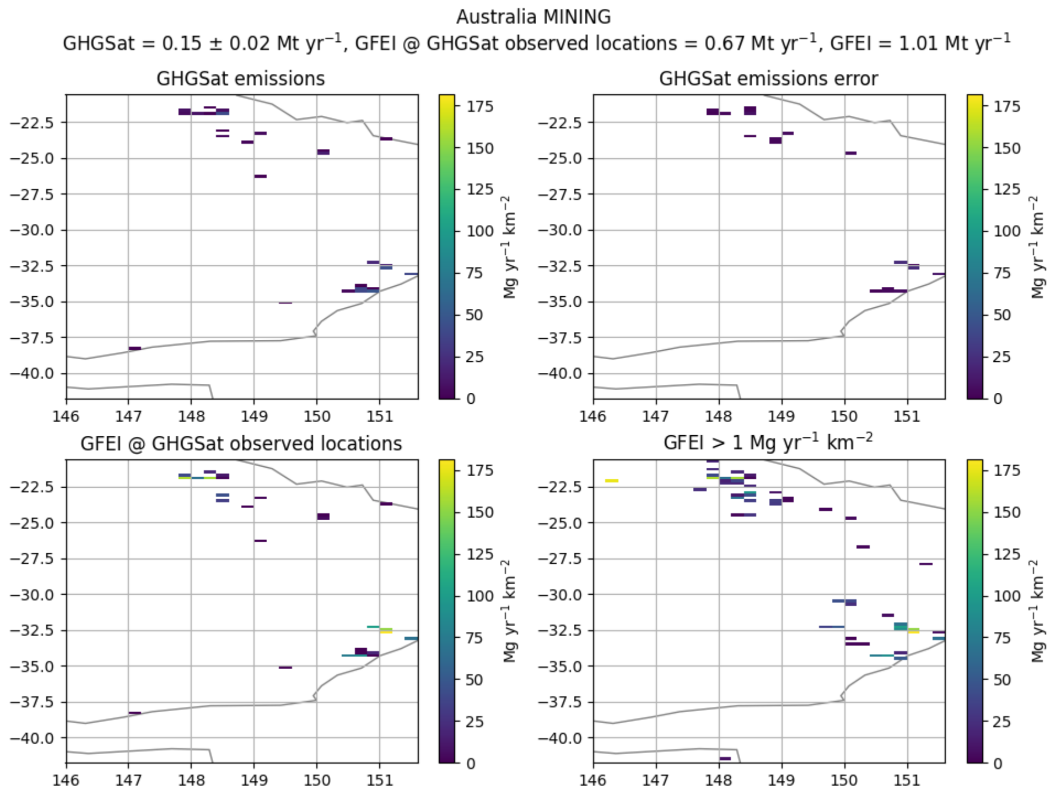


**Fig. S15.** Gridded GHGSat emissions (top left), GHGSat emissions error (top right), GFEIv3 emissions estimate at GHGSat-observed locations (bottom left), and GFEIv3 emissions (bottom right) for the case of Australia's Coal sector.

| Measurement | Quantity | Comments |
|---|---|---|
| Time Period | January 1, 2023 – December 31, 2023 | |
| Satellites performing measurements during the time period | 8 | GHGSat-C1 to C5 (full time period), C6-8 (since 5-23). |
| Number of clear-sky retrievals processed | 32,928 (14,137) | Over all location (Only over O&G + coal locations observed to be emitting in 2023) |
| Number of O&G + coal plumes detected | 11,419 = 8,687 O&G + 2,732 coal | |
| Number of spatially aggregated sites | 3,114 = 2,744 O&G + 370 coal | According to the spatial aggregation criteria described in the text |
| Average number of observations per site | O&G: (Avg, Med) = (26, 19)<br>coal: (Avg, Med) = (17, 12) | |
| Site revisit time | O&G: (Avg, Med) = (10, 5) days<br>coal: (Avg, Med) = (16, 8) days | |
| GHGSat energy emissions estimate | $8.30 \pm 0.24$ Mt yr$^{-1}$ = $5.80 \pm 0.23$ Mt yr$^{-1}$ O&G + $2.50 \pm 0.06$ Mt yr$^{-1}$ coal | |
| GFEIv3 total energy emissions estimate | 74.3 Mt yr$^{-1}$ = 43.7 Mt yr$^{-1}$ O&G + 30.7 Mt yr$^{-1}$ coal | |
| GFEIv3 energy emissions estimate at GHGSat observed locations | 34.1 Mt yr$^{-1}$ = 16.4 Mt yr$^{-1}$ O&G + 17.8 Mt yr$^{-1}$ coal | |
| Average site persistence | O&G: 0.15; coal: 0.48 | Average of the estimated persistence distribution, described in text. |

**Table S1**. Summary of GHGSat measurement details for this study.

| Country | GHGSat Q O&G [Mt/yr] | GHGSat Q error O&G [Mt/yr] | GHGSat Q Coal [Mt/yr] | GHGSat Q error Coal [Mt/yr] | GFEI Q O&G [Mt/yr] | GFEI Q Coal [Mt/yr] | GFEI Q O&G @ GHGSat observed locations [Mt/yr] | GFEI Q Coal @ GHGSat observed locations [Mt/yr] |
|---|---|---|---|---|---|---|---|---|
| Turkmenistan | 1.66 | 0.09 | 0 | 0 | 1.49 | 0 | 0.67 | 0 |
| China | 0.1 | 0.01 | 1.23 | 0.04 | 1.21 | 21.16 | 0.22 | 12.22 |
| Russia | 0.68 | 0.18 | 0.47 | 0.03 | 3.75 | 2.57 | 0.66 | 1.59 |
| United States | 0.91 | 0.06 | 0.11 | 0.01 | 8.48 | 1.88 | 4.12 | 0.94 |
| Mexico | 0.53 | 0.08 | 0 | 0 | 1.09 | 0.05 | 0.51 | 0.02 |
| Kazakhstan | 0.3 | 0.04 | 0.08 | 0.01 | 0.21 | 0.28 | 0.08 | 0.24 |
| Australia | 0.1 | 0.01 | 0.15 | 0.02 | 0.28 | 1.01 | 0.17 | 0.67 |
| Ukraine | 0.1 | 0.01 | 0.1 | 0.01 | 1.49 | 0.43 | 0.59 | 0.09 |
| Algeria | 0.18 | 0.02 | 0 | 0 | 1.01 | 0 | 0.43 | 0 |
| Poland | 0 | 0 | 0.17 | 0.01 | 0.11 | 0.57 | 0.01 | 0.56 |
| India | 0.08 | 0.01 | 0.09 | 0.01 | 0.87 | 0.91 | 0.16 | 0.82 |
| Uzbekistan | 0.16 | 0.02 | 0 | 0 | 1.42 | 0.01 | 0.28 | 0 |
| Iran | 0.15 | 0.02 | 0 | 0 | 2.83 | 0.02 | 1.31 | 0 |
| Syria | 0.1 | 0.01 | 0 | 0 | 0.05 | 0 | 0.03 | 0 |
| Pakistan | 0.08 | 0.01 | 0 | 0 | 0 | 0 | 0 | 0 |
| Nigeria | 0.07 | 0.03 | 0 | 0 | 3.04 | 0 | 0.58 | 0 |
| Yemen | 0.06 | 0.01 | 0 | 0 | 0.02 | 0 | 0.01 | 0 |
| Trinidad and Tobago | 0.06 | 0.02 | 0 | 0 | 0.08 | 0 | 0.05 | 0 |
| Bahrain | 0.06 | 0.01 | 0 | 0 | 0.21 | 0 | 0.21 | 0 |
| Iraq | 0.05 | 0.01 | 0 | 0 | 2.67 | 0 | 1.81 | 0 |
| Libya | 0.04 | 0.01 | 0 | 0 | 0.29 | 0 | 0.2 | 0 |
| Philippines | 0 | 0 | 0.04 | 0.01 | 0.01 | 0.02 | 0 | 0 |
| Venezuela | 0.03 | 0.01 | 0 | 0 | 0.78 | 0 | 0.31 | 0 |
| Egypt | 0.03 | 0 | 0 | 0 | 0.43 | 0 | 0.23 | 0 |
| Indonesia | 0.02 | 0 | 0.01 | 0 | 0.54 | 0.12 | 0.08 | 0.05 |
| Azerbaijan | 0.03 | 0 | 0 | 0 | 0.44 | 0 | 0.34 | 0 |
| Canada | 0.02 | 0.01 | 0 | 0 | 1.28 | 0.04 | 0.67 | 0.03 |
| South Africa | 0.01 | 0 | 0.01 | 0 | 0.07 | 0.07 | 0 | 0.05 |
| Kuwait | 0.02 | 0.01 | 0 | 0 | 0.14 | 0 | 0.13 | 0 |
| Argentina | 0.02 | 0 | 0 | 0 | 0.34 | 0 | 0.15 | 0 |
| Colombia | 0 | 0 | 0.02 | 0.01 | 0.25 | 0.2 | 0.09 | 0.17 |
| Mongolia | 0 | 0 | 0.02 | 0.01 | 0.01 | 0.04 | 0 | 0.02 |
| Oman | 0.02 | 0.01 | 0 | 0 | 0.23 | 0 | 0.14 | 0 |
| Mozambique | 0.02 | 0 | 0 | 0 | 0.01 | 0.02 | 0 | 0.02 |
| Qatar | 0.01 | 0 | 0 | 0 | 0.14 | 0 | 0.07 | 0 |
| Saudi Arabia | 0.01 | 0 | 0 | 0 | 0.45 | 0 | 0.2 | 0 |
| Brazil | 0.01 | 0 | 0 | 0 | 0.19 | 0.05 | 0.14 | 0.04 |
| Italy | 0.01 | 0.01 | 0 | 0 | 0.13 | 0 | 0.03 | 0 |
| Romania | 0.01 | 0 | 0 | 0 | 0.1 | 0.22 | 0.02 | 0.03 |

| | | | | | | | | |
|---|---|---|---|---|---|---|---|---|
| Brunei | 0.01 | 0.01 | 0 | 0 | 0.1 | 0 | 0.03 | 0 |
| South Sudan | 0.01 | 0 | 0 | 0 | 0.02 | 0 | 0.02 | 0 |
| Jordan | 0.01 | 0 | 0 | 0 | 0.02 | 0 | 0 | 0 |
| Germany | 0 | 0 | 0 | 0 | 0.19 | 0.01 | 0.03 | 0.01 |
| Czech Republic | 0 | 0 | 0 | 0 | 0.02 | 0.08 | 0 | 0.03 |
| France | 0 | 0 | 0 | 0 | 0.04 | 0 | 0 | 0 |
| Chad | 0 | 0 | 0 | 0 | 0.07 | 0 | 0.07 | 0 |
| Spain | 0 | 0 | 0 | 0 | 0.01 | 0 | 0 | 0 |
| Malaysia | 0 | 0 | 0 | 0 | 0.92 | 0 | 0.02 | 0 |
| New Zealand | 0 | 0 | 0 | 0 | 0.02 | 0 | 0 | 0 |
| South Korea | 0 | 0 | 0 | 0 | 0.2 | 0.01 | 0.05 | 0 |
| Peru | 0 | 0 | 0 | 0 | 0.08 | 0 | 0.04 | 0 |
| Japan | 0 | 0 | 0 | 0 | 0.01 | 0.02 | 0 | 0 |
| Austria | 0 | 0 | 0 | 0 | 0.01 | 0 | 0 | 0 |
| United Arab Emirates | 0 | 0 | 0 | 0 | 1.46 | 0 | 0.54 | 0 |
| Chile | 0 | 0 | 0 | 0 | 0.04 | 0 | 0.02 | 0 |
| Ecuador | 0 | 0 | 0 | 0 | 0.04 | 0 | 0.02 | 0 |
| Tunisia | 0 | 0 | 0 | 0 | 0.02 | 0 | 0.01 | 0 |
| Angola | 0 | 0 | 0 | 0 | 0.77 | 0 | 0.37 | 0 |

**Table S2.** National GHGSat emission estimates in 2023